Masterarbeit in Physik
angefertigt im
Helmholtz - Institut für Strahlen- und Kernphysik

Implantation studies on silicon doped group-III nitride semiconductors

vorgelegt der
Mathematisch-Naturwissenschaftlichen Fakultät
der
Rheinischen Friedrich-Wilhelms-Universität Bonn

von
Ronnie Ernst Simon

Bonn, September 2011

Masterarbeit in Physik
angefertigt im
Helmholtz - Institut für Strahlen- und Kernphysik

Implantation studies on silicon doped group-III nitride semiconductors

vorgelegt der
Mathematisch-Naturwissenschaftlichen Fakultät
der
Rheinischen Friedrich-Wilhelms-Universität Bonn

von
Ronnie Ernst Simon

Bonn, September 2011

1. Gutachter: Priv. Doz. Dr. Reiner Vianden

2. Gutachter: Prof. Dr. Kai-Thomas Brinkmann

Contents

1. Introduction 1

2. Gallium nitride 3
- 2.1 Sample material 3

3. Experimental method 7
- 3.1 Theoretical background 7
  - 3.1.1 The unperturbed angular correlation 7
  - 3.1.2 The hyperfine interaction 9
  - 3.1.3 The perturbed angular correlation 11
- 3.2 Experimental setup 14
- 3.3 Data analysis 16
- 3.4 PAC probes 18

4. Sample preparation 21
- 4.1 Ion implantation 21
- 4.2 Annealing of implantation damage 22
- 4.3 PAC furnace 23

5. Measurements 25
- 5.1 Time resolution of the PAC spectrometer 25
- 5.2 Annealing behaviour 27
  - 5.2.1 Undoped GaN: GN5465 27
  - 5.2.2 Highly doped GaN-Si: GN4885 28
  - 5.2.3 Discussion 31
- 5.3 Determination of the symmetry of the electric field gradient 35
- 5.4 Influence of the silicon concentration on the hyperfine fields at room temperature 37
  - 5.4.1 Results 37
  - 5.4.2 Discussion 38

5.5 Temperature dependent measurements 43
5.5.1 Results 43
5.5.2 Discussion 47

6. Summary 51

7. Outlook 53

Appendix 55

A. Tables 57
A.1 Annealing behaviour 57
A.2 Temperature dependent measurements 59

B. Spectra 63
B.1 Annealing behaviour 63
B.2 Temperature dependent measurments 65

Bibliography 75

Acknowledgement 77

1. Introduction

Group-III nitride semiconductors, especially gallium nitride (GaN), have drawn much attention in the last years. This is attributed to a wide range of applications [1]:
One remarkable feature of these materials is the formation of continuous alloy systems, e.g. $In_xGa_{1-x}N$, in which the optical bandgap can be tailored by varying the concentrations of the constituents. For example, in GaN and InN the energy bandgap is 3.4 eV and 1.9 eV, respectively, so the whole range of the visible spectrum can be covered. This makes group-III nitrides ideal for optoelectronic devices [2].
Due to a rapid development of growth techniques in the last years, high-quality epilayers and bulk single crystals are now commercially available. The successfull fabrication of both n- and p-type GaN led to excellent p-n-junctions, which are used for high-brightness green, blue and white LEDs in solid state lighting and outdoor displays. The p- and n-type conductivity of GaN are achieved by doping with magnesium and silicon (Si), respectively.
Owing to a high bond energy of 8.92 eV/atom, GaN exhibits a melting point of 2773 K and a significant radiation hardness. Furthermore, it is insoluble in water, acids and bases. This makes GaN an excellent candidate for device operation in high-temperature, caustic and radioactive environments. Due to a large breakdown field and high electron drift velocities, GaN is also used for the fabrication of high-power devices. Other applications of GaN include continuous wave lasers, UV detectors, laser diodes, solar cells and high electron mobility transistors for wireless devices.
Due to its wurtzite crystal structure, GaN has a non-symmetric charge distribution, which causes an electric field gradient. This electric field gradient interacts with the electric quadrupole moment of probe nuclei inside GaN. This makes the perturbed γ-γ-angular correlation technique a suitable investigation method. The radioactive probe nuclei ^{111}In are introduced into the sample material by ion implantation. So, the perturbed angular correlation method can also be applied for studying the annealing of implantation damage.
One aim of this thesis is to investigate, how the hyperfine fields in GaN are affected by the charge carrier density. Previous studies on ^{111}In in GaN and AlN showed that crystal defects, probably nitrogen vacancies, and indium atoms form a bond [3]. This defect-indium bond was found to be stable up to 500 K. The investigation of the influence of the charge carrier density on this bond is a second

aim of this study. Another part of this thesis is focused on the effect of doping on the annealing behaviour after ion implantation and stability of GaN films at high temperatures.
For this purpose, silicon doped GaN films with concentrations ranging from 2×10^{17} atoms/cm^3 to 9.2×10^{18} atoms/cm^3 are investigated. An undoped GaN film is used as a reference. All films were fabricated using the same growth technique to assure comparability. When GaN is doped with silicon (Si), the Si-atoms replace Ga-atoms in the lattice. Since silicon is a group-IV element, it acts as a donor on the Ga-site and contributes with one extra electron to the conduction band [4]. Hall effect measurements showed that free charge carrier density is essentially increased and in the order of the silicon concentration [5].

Chapter 2 gives a short overview on the relevant properties of GaN and the investigated samples in particular. Chapter 3 is dedicated to the experimental method of the perturbed angular correlation. Both the theoretical background and the experimental setup are described. In Chapter 4, the sample preparation is described. The results of the measurements are presented and discussed in Chapter 5.

2. Gallium nitride

2.1 Sample material

The material investigated in this study is based on gallium nitride (GaN). A comprehensive overview about the properties of GaN is given in the textbook of Morkoç [1]. GaN crystallizes in the wurtzite and in the zinc blende structure, whereas only the former is thermodynamically stable under normal conditions [6]. In the wurtzite structure, the gallium and nitrogen atoms seperately form a hexagonal closed-packed sublattice with lattice constants a and c. These sublattices are shifted along the c-direction about the distance b. The shift is characterized by the u-parameter, which is defined as the displacement in units of the lattice constant c: $u = b/c$. Every atom has four nearest neighbours, which are atoms of the other sublattice, at the corners of a tetrahedron. The wurtzite structure is shown Figure 2.1.
In an ideal wurtzite structure, all bonding lengths are equal to each other and each atom is located in a perfect tetrahedral environment. The ratio between the two lattice constants is $c/a = \sqrt{8/3} = 1.633$ and the u-parameter is $u = 3/8 = 0.375$. As one can learn from Table 2.1, in GaN the c/a ratio and the u-parameter deviate from the ideal values. Therefore, the bonding lengths in a- and c-direction are different from each other and a non-symmetrical charge distribution can be found in GaN. This leads to an intrinsic electric field gradient (EFG), which is axially symmetric with respect to the c-direction.
Some important properties of GaN are summarized in Table 2.1.

Lattice constant a	3.1872(1) Å
Lattice constant c	5.1818(1) Å
c/a ratio	1.62582(6)
u-parameter	0.3772(2)
density	6.15 g/cm^3
atomic density	8.79×10^{22} atoms/cm^3
Energy bandgap at 300 K	3.4 eV
melting point	2773 K

Tab. 2.1: Some important properties of GaN. Values are taken from [1], [7] and [8].

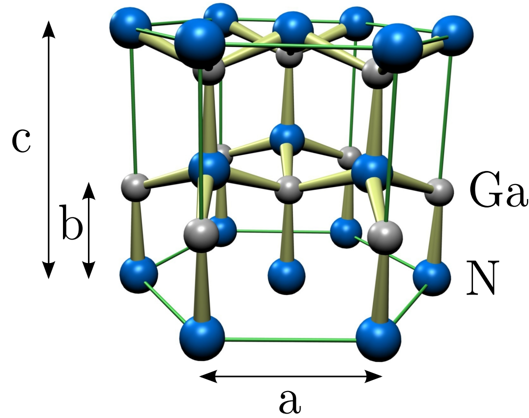

Fig. 2.1: The wurtzite structure of GaN.

The fabrication of GaN films can be achieved by several crystal growth techniques. All the samples investigated in this study were grown using the metal organic vapour phase epitaxy (MOVPE) technique by Ambacher and Köhler from the Fraunhofer institute for applied solid-state physics (IAF) in Freiburg. The films are monocrystalline and grown such that the c-axis of the crystal is perpendicular to the surface.
A comprehensive description of growth techniques for group-III nitrides can be found in the review article by Ambacher [9] or the textbook by Morkoç [1]. The basic principle of MOVPE is the following. Precursor gases containing the required chemical elements are introduced into a reactor chamber, where they react on the surface of a heated substrate. During the growth process gas pressure, flow rates and temperature play a crucial role. GaN layers can be grown using the precursor gases trimethylgallium ($Ga(CH_3)_3$) and ammonia (NH_3). By adding a third precursor gas doping with impurities can be achieved. For silicon doping silane (SiH_4) can be used. The doping concentration can be varied by changing the flow rate [1].
A major drawback of GaN is that native substrates are not yet available in large quantities. However, GaN can be grown on silicon carbide (SiC) or sapphire (Al_2O_3). Despite a large lattice mismatch of 13.9 % and a thermal expansion mismatch of 25.5 % [9] sapphire is the most popular substrate, because it is widely available and has low production costs. The thermal and structural mismatches introduce residual stress upon cooling the films after growth [9].

For this study silicon doped GaN films with five different concentrations ranging from 2×10^{17} atoms/cm^3 to 9.2×10^{18} atoms/cm^3 are available. The films are grown on sapphire. In order to improve the crystal quality, an undoped GaN buffer layer of 2 μm thickness is first grown on the substrate. On top of that a silicon doped GaN layer with a thickness ranging from 890 nm to 970 nm is grown. The layer

structure is shown Figure 2.2. Additionally, an undoped GaN film (GN5465) of 2.4 μm thickness is used as a reference. The silicon concentration and thickness of the doped layer were measured by Ambacher and Köhler using secondary ion mass spectroscopy (SIMS). The results can be found in Table 2.2.

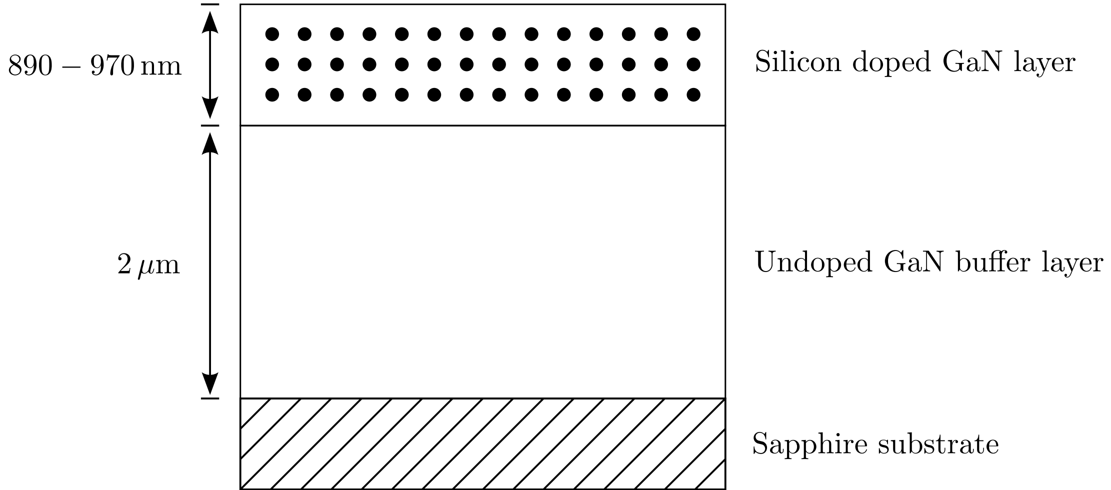

Fig. 2.2: The layer structure of the silicon doped GaN samples.

Epitaxy-Number	Si-Concentration [atoms/cm^3]	layer thickness [nm]
GN5499	2×10^{17}	890
GN4895	6×10^{17}	980
GN4877	1.1×10^{18}	900
GN4876	3.7×10^{18}	900
GN4885	9.2×10^{18}	970

Tab. 2.2: Silicon concentration and thickness of the doped layer measured with SIMS.

3. Experimental method

3.1 Theoretical background

The perturbed angular correlation method (PAC) is an experimental technique in nuclear solid state physics. It is based on the hyperfine interaction between a radioactive probe atom and fields present at the position of the probe atom. In more detail, the nuclear electric quadrupole and magnetic dipole moment interact with electric field gradients and magnetic fields. For example an electric field gradient can originate from the charge distribution in a non-cubic crystal lattice like the wurtztite structure, which can be found in many group-III nitride semiconductors. Crystal defects like substitutional and interstitial impurities or vacancies also lead to an electric field gradient. This, for example, allows to investigate lattice damage, which occurs during ion implantation. Experimentally, the hyperfine interaction is observed by a time dependent change of the angular correlation between two successive γ-rays in a γ-γ-cascade due to an external perturbation.

The approach of this chapter is based upon the textbook by Schatz and Weidinger [10]. A comprehensive description of the theory of the perturbed angular correlation can be found in the textbook by Siegbahn [11]. In this chapter, first the unperturbed angular correlation is considered. Afterwards the hyperfine interaction in a static electric field gradient, which causes a perturbation of the angular correlation, is discussed. The last part of this section is dedicated to the perturbed angular correlation.

3.1.1 The unperturbed angular correlation

A typical decay scheme of a γ-γ-cascade is depicted in Figure 3.1. A nucleus decays from the inital state $|I_i, M_i\rangle$ to an intermediate state $|I, M\rangle$ by emission of a γ-ray γ_1. This is followed by a transition to the final state $|I_f, M_f\rangle$ and the emission of a second γ-ray γ_2. Each γ-ray possesses a defined angular momentum quantum number $l_{1,2}$ and a magnetic quantum number $m_{1,2}$. Angular momentum conservation leads to the following restrictions for the transitions.

$$|l_1 - I| \leq I_i \leq |l_1 + I| \qquad M_i = m_1 + M \tag{3.1}$$

$$|l_2 - I_f| \leq I \leq |l_2 + I_f| \qquad M = m_2 + M_f \tag{3.2}$$

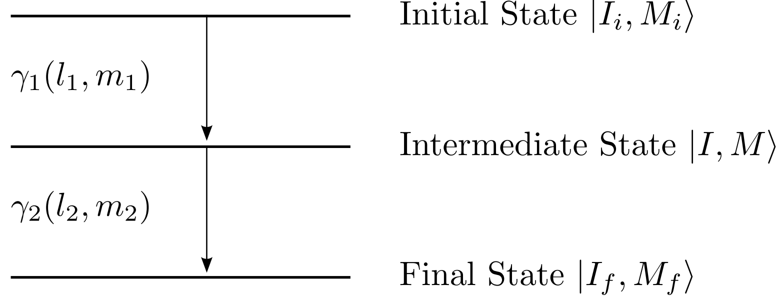

Fig. 3.1: A typical decay scheme of a γ-γ-cascade. A nucleus decays from the intial state $|I_i, M_i\rangle$ via an intermediate state $|I, M\rangle$ to the final state $|I_f, M_f\rangle$ by the emission of two γ-rays.

Every emission of a γ-ray obeys a certain angular distribution $F_{lm}(\theta)$ relative to the orientation of the nuclear spin given by its quantum numbers. $F_{lm}(\theta)$ is essentially given by spherical harmonics Y_l^m, where θ is the angle between the z-axis and the direction of emission and $\vec{L}$ is the total angular momentum operator.

$$F_{lm}(\theta) = \frac{\left|\vec{L}Y_l^m\right|^2}{\sum_m \left|\vec{L}Y_l^m\right|^2} \tag{3.3}$$

When in an experiment a large number of nuclei is considered, the directions of the nuclear spins are randomly distributed. Therefore, every direction of emission for one single γ-ray has the same probability and the observed angular distribution is isotropic. In the case of a γ-γ-cascade the direction of emission of the second γ-ray is correlated to the first γ-ray, because the second is emitted from a state, which was populated by the first, and angular momentum is conserved. By detecting the first γ-ray in an arbitrary but fixed direction $\vec{k}_1$ and the second one in a direction $\vec{k}_2$ in coincidence, a defined angular correlation $W(\vec{k}_1, \vec{k}_2)$ between the two γ-rays can be observed. It is given by the transition amplitudes for the two γ-rays.

$$W(\vec{k}_1, \vec{k}_2) = \sum_{M_i, M_f, \sigma_1, \sigma_2} \left| \sum_M \langle I, M, \vec{k}_1, \sigma_1 | H_1 | I_i, M_i \rangle \langle I_f, M_f, \vec{k}_2, \sigma_2 | H_2 | I, M \rangle \right|^2 \tag{3.4}$$

H_1 and H_2 are the operators inducing the transitions. σ_1 and σ_2 are the polarizations of the γ-rays. The outer summation has to be done incoherently, because in principle one can measure the polarizations and the different sublevels $|M_{i,f}\rangle$ of the initial and final state. The inner summation over the sublevels $|M\rangle$ of the intermediate state has to be done coherently, since it is not possible to distinguish between them.

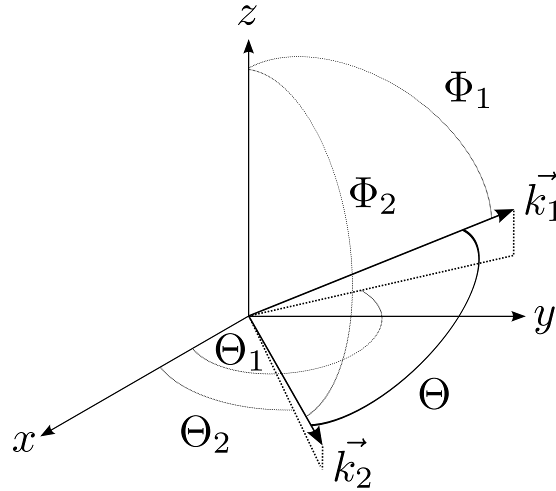

Fig. 3.2: The first γ-ray is detected in the direction $\vec{k_1}$ and the second in the direction $\vec{k_2}$. The angular correlation of the two γ-rays depends on the angle θ between $\vec{k_1}$ and $\vec{k_2}$.

Calculation of the matrix elements and the sums leads to the formula for the unperturbed angular correlation:

$$W(\vec{k_1}, \vec{k_2}) = W(\theta) = \sum_{k\ even}^{k_{max}} A_{k_1}(1) A_{k_2}(2) P_k(\cos\theta), \tag{3.5}$$

with θ being the angle between $\vec{k_1}$ and $\vec{k_2}$ (see Figure 3.2). The $P_k(\cos\theta)$'s are the Legendre polynoms. The so-called anisotropy coefficients $A_{k_1}(1)$ and $A_{k_2}(2)$ depend on the nuclear spins of the states in the cascade and the quantum numbers of the γ-rays. They can be derived from Clebsch-Gordon-Coefficients. For one given cascade these coefficients are constant and tabulated [12]. The summation index k is restricted to all even values

$$0 \leq k \leq \mathrm{Min}\left[2I, \mathrm{Max}\left(2l_1, 2l_1'\right), \mathrm{Max}\left(2l_2, 2l_2'\right)\right], \tag{3.6}$$

where $l_{1,2}$ and $l'_{1,2}$ are the angular momentum quantum numbers for mixed transitions. These restrictions are due to the coupling of angular momenta for the two transitions.

3.1.2 The hyperfine interaction

This study focuses on the interaction with electric field gradients. Therefore, the following discussion of the hyperfine interaction describes the electric interactions in more detail.

Inside a crystal lattice an electric potential $\phi(\vec{r})$ exists, which two parts contribute

to. The first contribution is given by the ions of the lattice and the second one by the charge distribution of the electrons. When a nucleus is subjected to this electric potential, an interaction between the charge distribution $\rho(\vec{r})$ of the nucleus with the potential $\phi(\vec{r})$ occurs. The interaction energy is given by the expression:

$$E = \int \phi(\vec{r})\rho(\vec{r})d^3r \qquad \text{with} \qquad \int \rho(\vec{r})d^3r = Ze, \tag{3.7}$$

where Ze is the total charge of the nucleus. The potential can be expanded into a Taylor series around the position of the nucleus. The constant term E_0 of the expansion describes the Coulomb interaction of a point charge in an electric field. This term does not depend on the nuclear spin or its magnetic quantum number M. As a consequence, due to E_0 there is only a constant shift and not a splitting of the $|M\rangle$-sublevels of the intermediate states.
The linear term of the expansion describes the interaction of the dipole moment of the nucleus with the electric field. Since a nucleus possesses a vanishing electric dipole moment, which is due to the defined parity of the nucleus, the linear term does not contribute.
The quadratic term of the expansion yields the quadrupole interaction. The corresponding Hamiltonian H_Q can be calculated from the formula:

$$H_Q = \frac{4}{5}\pi \sum_{q=-2}^{2} (-1)^q Q_q V_{-q}. \tag{3.8}$$

Q_q and V_q are the tensor components of the electric quadrupole moment and electric field gradient, respectively. The V_q can be expressed in terms of cartesian gradients of the electric potential $\phi(\vec{r})$:

$$V_{ij} = \frac{\partial^2 \phi}{\partial i \partial j} \qquad \text{with} \qquad i, j = x, y, z. \tag{3.9}$$

By choosing a principal axis coordinate system, in which V_{ij} is diagonal, one gets the tensor components:

$$\begin{aligned} V_0 &= \frac{1}{4}\sqrt{\frac{5}{\pi}} V_{zz} \\ V_{\pm 1} &= 0 \\ V_{\pm 2} &= \frac{1}{4}\sqrt{\frac{5}{6\pi}} \eta V_{zz} \qquad \text{with} \qquad \eta = \frac{V_{xx} - V_{yy}}{V_{zz}}. \end{aligned} \tag{3.10}$$

η is called the asymmetry parameter. Since there is no charge at the position of the nucleus, the potential obeys the Poisson equation $\Delta\phi(\vec{r}) = V_{xx} + V_{yy} + V_{zz} = 0$. The electric field gradient is then fully described by the two parameters V_{zz} and η. It is convenient to choose the coordinate system such that $|V_{xx}| \leq |V_{yy}| \leq |V_{zz}|$.

For reasons of simplicity, an axial symmetric field gradient with respect to the z-axis is considered. The asymmetry parameter η vanishes in this case and the sum in Eq. 3.8 is reduced to one term:

$$H_Q = \sqrt{\frac{\pi}{5}} Q_0 V_{zz}. \tag{3.11}$$

The calculation of the matrix elements of this Hamiltonian in the $|M\rangle$-representation leads to:

$$\langle IM|H_Q|IM\rangle = E_M = \frac{3M^2 - I(I+1)}{4I(2I-1)} eQV_{zz}. \tag{3.12}$$

This term gives the energy of an $|M\rangle$-sublevel, when a nucleus with nuclear spin I and electric quadrupole moment Q is subjected to an axial symmetric electric field gradient. As E_M depends quadratically on M, the sublevels $|M\rangle$ and $|-M\rangle$ are degenerate.
It is convenient to introduce the so-called quadrupole frequency ω_Q and the quadrupole coupling constant ν_Q:

$$\omega_Q = -\frac{eQV_{zz}}{4I(2I-1)\hbar} \tag{3.13}$$

$$\nu_Q = \frac{eQV_{zz}}{h}. \tag{3.14}$$

The energy difference between two $|M\rangle$-sublevels can be written in terms of ω_Q.

$$E_M - E_{M'} = 3\left|M^2 - M'^2\right| \hbar\omega_Q \tag{3.15}$$

The angular frequency ω_0 corresponding to the smallest energy difference between the $|M\rangle$-sublevels is

$$\hbar\omega_0 = E_M - E_{M'} = \begin{cases} 3\omega_Q & \text{if } I \text{ is an integer} \\ 6\omega_Q & \text{if } I \text{ is an half integer.} \end{cases} \tag{3.16}$$

If the asymmetry parameter η is not zero, the splitting of the $|M\rangle$-sublevels will depend on η, as it is shown in Figure 3.3 for a spin of $I = 5/2$ [13]. In this case the Hamiltonian H_Q is not diagonal anymore and induces transitions between the $|M\rangle$-sublevels.

3.1.3 The perturbed angular correlation

When the intermediate state has a finite life time τ_N and the nucleus is subjected to a hyperfine interaction, a perturbation of the angular correlation $W(\theta)$ (Eq.

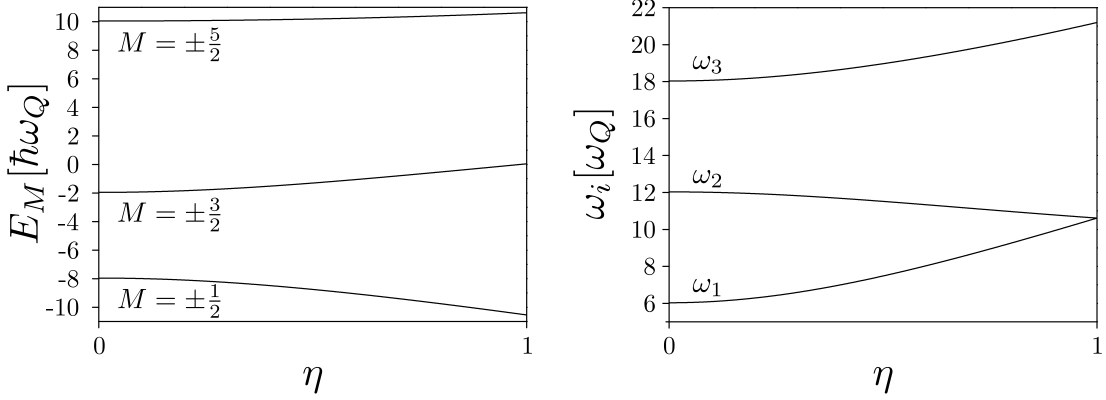

Fig. 3.3: Left: The energy E_M of the different $|M\rangle$-sublevels for a spin of $I = 5/2$ depending on η. Right: The frequencies corresponding to transitions between the $|M\rangle$-sublevels depending on η.

3.4) occurs. The hyperfine interaction can be described quantum mechanically by a time evolution operator

$$\Lambda(t) = \exp\left(-\frac{i}{\hbar} H_Q t\right), \tag{3.17}$$

with the perturbation Hamiltonian H_Q. The following discussion of the perturbation is valid for any given perturbation described by a Hamiltonian H_Q.

The time evolution operator acts on the $|M\rangle$-sublevels of the intermediate state.

$$|M\rangle \rightarrow \Lambda(t)\,|M\rangle = \sum_{M'} \langle M'|\Lambda(t)|M\rangle\,|M'\rangle \tag{3.18}$$

The perturbation induces a change in the population of the different $|M\rangle$-sublevels of the intermediate state, so that the second γ-ray is not emitted from the final state $|M\rangle$ of the first γ-ray but from a state $|M'\rangle$, as depicted in Figure 3.4. The formula for the unperturbed angular correlation (Eq. 3.4) has to be changed in such a way, that the time evolution operator $\Lambda(t)$ acts first on the intermediate state $|M\rangle$ and then the transition to the final state is induced by a Hamiltonian H_2.

$$W\left(\vec{k}_1, \vec{k}_2, t\right) = \sum_{M_i, M_f, \sigma_1, \sigma_2} \left| \sum_M \langle M|H_1|M_i\rangle\,\langle M_f|H_2\Lambda(t)|M\rangle \right|^2 \tag{3.19}$$

Here the short notation $\langle I, M, \vec{k}_1, \sigma_1|H_1|I_i, M_i\rangle \equiv \langle M|H_1|M_i\rangle$ for the first, and analogously for the second matrix element, is used in order to focus on the difference between the unperturbed and perturbed angular correlation. As can be seen, the angular correlation function is now time dependent.

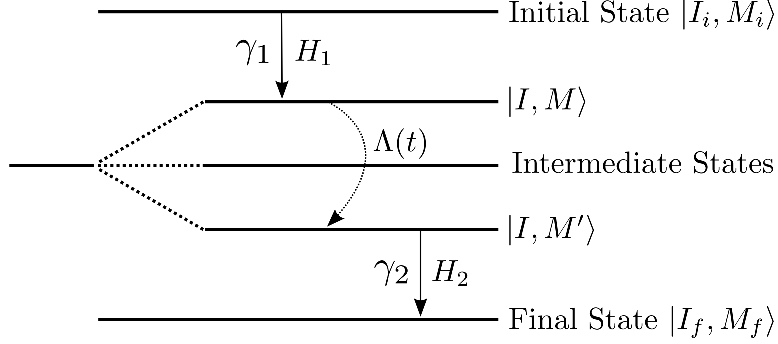

Fig. 3.4: A perturbation described by the time evolution operator $\Lambda(t)$ induces a transition between the intermediate $|M\rangle$-sublevels. The second γ-ray of the cascade is then emitted from a different state $|M'\rangle$. H_1 and H_2 are the Hamiltonians describing the emission of the γ-rays.

The further evaluation is rather complicated and should not be considered here. The finale result is the following.

$$W\left(\vec{k_1},\vec{k_2},t\right) = \sum_{k_1,k_2,N_1,N_2} A_{k_1}(1)A_{k_2}(2)G_{k_1k_2}^{N_1N_2}(t)\frac{Y_{k_1}^{N_1^*}(\theta_1,\phi_1)\,Y_{k_2}^{N_2}(\theta_2,\phi_2)}{\sqrt{(2k_1+1)(2k_2+1)}}, \quad (3.20)$$

where the perturbation factor is defined as

$$\begin{aligned} G_{k_1k_2}^{N_1N_2}(t) &= \sum_{M_a,M_a',M_b,M_b'} (-1)^{2I+M_a+M_b}\sqrt{(2k_1+1)(2k_2+1)} \\ &\quad \times \begin{pmatrix} I & I & k_1 \\ M_a' & -M_a & N_1 \end{pmatrix}\begin{pmatrix} I & I & k_2 \\ M_b' & -M_b & N_2 \end{pmatrix} \\ &\quad \times \langle M_b|\Lambda(t)|M_a\rangle\,\langle M_b'|\Lambda(t)|M_a'\rangle^*. \end{aligned} \quad (3.21)$$

Like for the unperturbed angular correlation function, the summation indices $k_{1,2}$ are restricted to $k_i = 0, 2, \ldots, \mathrm{Min}(2I, l_i + l_i')$ and $|N_i| \le k_i$. Eq. 3.20 is the general form of the perturbed angular correlation.

In the case of a statical and axial symmetric interaction, for example an electric field gradient axially symmetric relative to the z-axis, the perturbation factor (Eq. 3.21) can be simplified. The matrix elements of the time evolution operator in the $|M\rangle$-representation are given by

$$\langle M_b|\Lambda(t)|M_a\rangle = \exp\left[-\frac{i}{\hbar}E(M)t\right]\delta_{M,M_a}\delta_{M,M_b}. \quad (3.22)$$

From Eq. 3.22 one can see that the time evolution operator $\Lambda(t)$ is diagonal. Therefore, in this special case the perturbation does not lead to a change of the

population of the different $|M\rangle$-sublevels. Only the phase of the different states is changed. By inserting Eq. 3.22 into Eq. 3.21 one gets for the perturbation factor

$$\begin{aligned} G^{NN}_{k_1k_2}(t) &= \sum_{M,M'} \sqrt{(2k_1+1)(2k_2+1)} \begin{pmatrix} I & I & k_1 \\ M' & -M & N \end{pmatrix} \begin{pmatrix} I & I & k_2 \\ M' & -M & N \end{pmatrix} \\ &\quad \times \exp\left[-\frac{i}{\hbar}(E(M)-E(M'))t\right]. \end{aligned} \tag{3.23}$$

For an electric quadrupole interaction the energy difference $E(M) - E(M')$ is given by Eq. 3.16. The perturbation factor (Eq. 3.23) can be written in a more instructive way:

$$\begin{aligned} G^{NN}_{k_1k_2}(t) &= \sum_n s^{k_1k_2}_{nN} \cos(n\omega_0 t) \\ s^{k_1k_2}_{nN} &= \sum_{M,M'} \sqrt{(2k_1+1)(2k_2+1)} \begin{pmatrix} I & I & k_1 \\ M' & -M & N \end{pmatrix} \begin{pmatrix} I & I & k_2 \\ M' & -M & N \end{pmatrix}, \\ \text{with} \quad n &= \begin{cases} |M^2 - M'^2| & \text{if } I \text{ is an integer} \\ \frac{1}{2}|M^2 - M'^2| & \text{if } I \text{ is an half integer.} \end{cases} \end{aligned} \tag{3.24}$$

ω_0 is the frequency equivalent to the smallest energy difference of two $|M\rangle$-sublevels as defined in Eq. 3.16.
As a result, in the angular correlation function (Eq. 3.20) one observes a periodic change with frequencies $n\omega_0$.

Considering the isotope ^{111}In, the intermediate state of the cascade has a nuclear spin of $I = \frac{5}{2}$. This leads in total to three different frequencies corresponding to $M = \pm\frac{1}{2}$, $\pm\frac{3}{2}$ and $\pm\frac{5}{2}$. Using Eq. 3.15, these frequencies are in multiples of ω_Q:

$$\begin{aligned} \omega_1 &= 6\omega_Q \\ \omega_2 &= 12\omega_Q \\ \omega_3 &= 18\omega_Q. \end{aligned} \tag{3.25}$$

3.2 Experimental setup

In the last section it was shown that an electric field gradient leads to a time dependent change of the angular correlation between two γ-rays in a γ-γ-cascade. In a simplified picture, this corresponds descriptively to a rotation of the emission characteristics. When the two γ-rays are detected in coincidence with two detectors arranged at fix positions, the coincidence count rate changes periodically in time due to this rotation (see Figure 3.5).

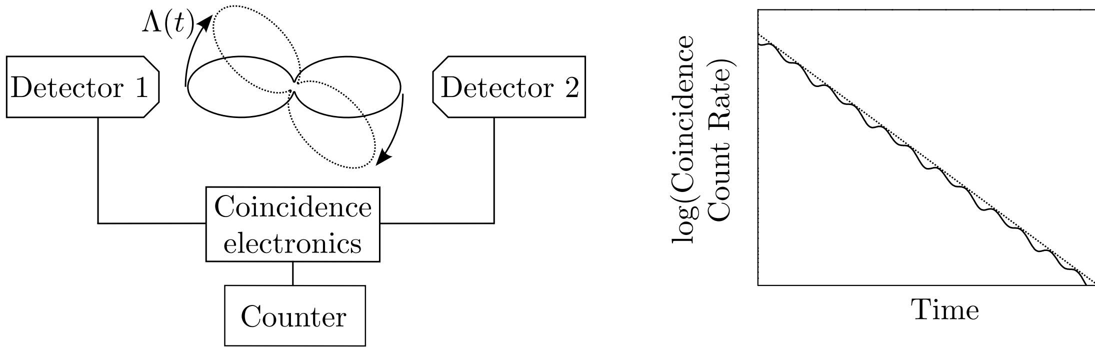

Fig. 3.5: When the two γ-rays are detected in coincidence with two fixed detectors, the measured coincident count rate changes periodically in time. The reason for the time-dependency is the rotation of the emission characteristics due to an electric field gradient.

The coincidence count rate is measured by means of a fast-slow-coincidence circuit. The measurements in this study are taken at two different detector systems. In the first Barium fluoride (BaF_2) and in the second lutetium oxyorthosilicate (Lu_2SiO_5:Ce^{3+} or LSO) is used as a scintillation material. Further details on these two systems can be found in the PhD theses of Koch [14] and Valentini [15]. In order to give an understanding of the basic principle of a fast-slow-coincidence, the BaF_2 detector system will be considered in the following.

A schematic view of the circuit is shown in Figure 3.6. The scintillation detectors are connected to photomultipliers, which provide a fast and a slow output signal. The fast signal has a good time resolution whereas the slow signal possesses a good energy resolution.

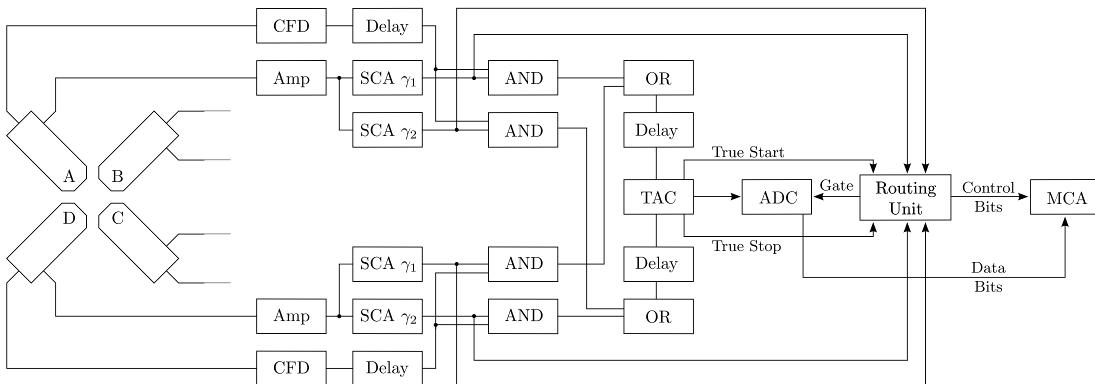

Fig. 3.6: A schemativ view of the fast-slow-coincidence circuit. For reasons of simplicity only the electronics for two detectors are shown.

The slow signal is filtered by a single channel analyzer (SCA), in order to select only those γ-rays, which have the right energies for the γ-γ-cascade. Each detector

can thereby measure the first or the second γ-ray. Fur this purpose, the slow signal is splitted and two SCAs are connected to each detector. A routing unit (coincidence unit) is used to check whether the two detected γ-rays are emitted from the same nucleus. If this is the case, the routing unit will give a logic signal to the gate input of the analog-to-digital converter (ADC) to permit writing data into the multichannel-analyzer (MCA).
The fast signal is analysed with a constant fraction discriminator (CFD), which converts the incoming pulse into a logic signal. These pulses serve as start and stop signals for the time measurement. The time measurement is done by a time-to-amplitude converter (TAC). In order to reduce the deadtime of the TAC, the CFD-signals are delayed by 200 m long cables, which corresponds to a time delay of $\approx 1\,\mu$s, and checked by an AND gate for being coincident with the output signals of the SCAs.
Due to the fact that four detectors allow for twelve possible start and stop combinations the routing unit shifts all measurements relative to each other by the help of control bits. By doing so, twelve seperate time measurements each with 2048 channels are obtained.

In contrast, the LSO-detectors provide only one output for the time and the energy signal. In this system, fast constant fraction differential discriminators (CFDD) can be applied, which have a built-in SCA. The advantage of the LSO-detectors is a higher detection efficiency due to a larger density and larger effective atomic number of the scintillation material. For that reason, the energy resolution is higher compared to BaF_2-scintillators. However, the disadvantage is that the lutetium fraction of the LSO is composed of the stable isotope ^{175}Lu and the long-lived beta-radioactive isotope ^{176}Lu. This leads to immediate random coincidences and one gets a prompt peak at the beginning of the time measurement. These peaks are taken as the starting points in time. This fact has to be taken into account in the data analysis.

3.3 Data analysis

As depicted in Figure 3.6, neighbouring detectors are at an angle of 90° relative to each other. In this study, a four detector setup is used with an angle of 90° between neighbouring detectors. Each detector seperately detects the start signal, i.e. the first γ-ray, and the stop signal, i.e. the second γ-ray, for the time measurement. Since there are four detectors, in total twelve start and stop combinations are possible; four combinations with the detectors at an angle of 180° to each other and eight at an angle of 90°. Each coincidence count rate N_i between two detectors is given by

$$N_i(\theta, t) = N_{0,i} \exp\left(-\frac{t}{\tau}\right) W(\theta, t) + U_i. \tag{3.26}$$

The first term gives the radioactive decay of the probe nuclei multiplied by the time dependent angular correlation function $W(\theta, t)$, which describes the probability of measuring the two γ-rays with the detectors at angle θ and at a time t. τ is the life time of the intermediate state. The second term U_i describes the measured background due to random coincidences.

The time zero points representing the time $t = 0\,\text{s}$, when the first γ-ray of the cascade is detected, have to be determined manually, because all spectra are shifted relative to each other. On the one hand, this can be achieved by using a ^{60}Co calibration source. On the other hand, one can use the program *TZCal*, developed by Nédélec [16], to set the time zero points.
Each detector possesses a unique detection efficiency and amplification. Therefore, the detected random coincidences are different for every detector combination. The program *Showfit*, developed by Ruske [17], is applied to correct each coincidence count rate for the background. This is done by fitting an exponential life time curve to the data having the life time of the intermediate state.
All the information about the perturbation is contained in the angular correlation function and in the perturbation factor (see Eq. 3.24), in particular. For evaluating the perturbation the so-called $R(t)$-value is calculated by means of the program *Showfit*:

$$R(t) = 2\frac{\overline{N}(180\,^\circ, t) - \overline{N}(90\,^\circ, t)}{\overline{N}(180\,^\circ, t) + 2\overline{N}(90\,^\circ t)}, \tag{3.27}$$

where $\overline{N}(\theta, t)$ is the geometric mean of the background corrected coincidence count rates. The exponential fraction is thereby seperated from the coincidence count rate and a normalized angular correlation function remains. Since $R(t)$ describes the difference between the coincidence count rates for a parallel and a perpendicular detector orientation, $R(t)$ is called the anisotropy. A detailed overview about different data evaluation methods for PAC can be found in the article by Arends et al. [18].

When probe nuclei in a sample are located in different types of electronic environments, they are subjected to an EFG characteristic for the corresponding type of environment. Each type of environment contributes with a distinct angular correlation $W_i(\theta_i, t)$ to the measured angular correlation $W(\theta, t)$:

$$W(\theta, t) = \sum_i W_i(\theta_i, t) f_i \qquad \sum_i f_i = 1 \tag{3.28}$$

The weighting factor f_i gives the percental fraction of probe atoms in a certain type of environment.
When the EFGs in one type of electronic environment slighty differ from each other in magnitude, similar but not equal frequencies contribute to the angular correlation function W_i. The summation of all these frequency contributions leads

to a reduction or damping of W_i over time. Mathematically, this can be described by multiplying W_i by a frequency distribution $\exp(-\overline{\omega}\delta t)$ with a mean frequency $\overline{\omega}$ of Lorentzian shape with width δ. δ is referred to as the damping of the fraction.

The program *Nightmare*, designed by Nédélec [16], is applied to analyse the data. It allows to consider different angular correlation functions W_i, whereas each function is characterized by a set of fit parameters: the percental fraction f_i, the frequency $\omega_{0,i}$, the asymmetry parameter η_i, the damping δ_i and the angle θ_i between the detector and the electric field gradient. Additionally, in *Nightmare* it is possible to consider environments, in which the electric field gradient is randomly oriented as in polycrystalline samples. The total angular correlation function $W(\theta,t) = \sum_i W_i(\theta,t)$ is fitted to the $R(t)$ spectrum using a least squares fit.

The anisotropy coefficients $A_{k_1}(1)A_{k_2}(2)$ (see Eq. 3.20) depend on the solid angle covered by the detectors. This leads to deviation of the measured coefficients $A_{k_1}(1)A_{k_2}(2)$ from the theoretical values. Therefore, in the fitting routine corrected values for the $A_{k_1}(1)A_{k_2}(2)$ are used [16].

3.4 PAC probes

There are several requirements to isotopes for being an appropriate PAC-probe. First of all, the isotope should decay via a γ-γ-cascade. The half life of the intermediate state should be in the range from ns to μs. The lower limit of the half life is determined by the time resolution of the detector setup. If the half life is too long, the probability of measuring the second γ-ray from a different nucleus will increase and consequently the measured background will be to high. The time window (PAC window) during which the angular correlation can be observed is determined by the half life and is usually several half lives long. Since the interaction frequency is proportional to the quadrupole moment Q (see Eq. 3.13), Q should be larger than 0.1 b to observe the time dependence of the angular correlation during the PAC window. Furthermore, the anisotropy coefficients $A_{k_1}(1)A_{k_2}(2)$ of the cascade should be large.
The half life of the parent isotope should be reasonably long to allow for sample preparation and several measurements.

All measurements in this study are taken using the isotope ^{111}In, which is a well-known PAC-probe and fulfills all the requirements. ^{111}In decays via electron capture to a excited state of ^{111}Cd with a nuclear spin of $I_i = 7/2$. The nucleus decays subsequently to an intermediate state with a spin of $I = 5/2$ by emitting a γ-ray with an energy of 171 keV. The electric quadrupole moment of this state is

$Q = 0.83(13)$ b. Eventually, a γ-ray with an energy of 245 keV is emitted and the nucleus is situated in the ground state with a spin of $I_f = 1/2$. The anisotropy coefficients are $A_2(1)A_2(2) = -0.17$ and $A_2(1)A_4(2) = -0.204$. The decay scheme of the γ-γ-cascade in ^{111}In is shown in Figure 3.7.

Since In is a group-III element like Ga, it shows a similar chemical behaviour and only the different atomic radii have to be considered, when In is used as a PAC-probe in GaN.

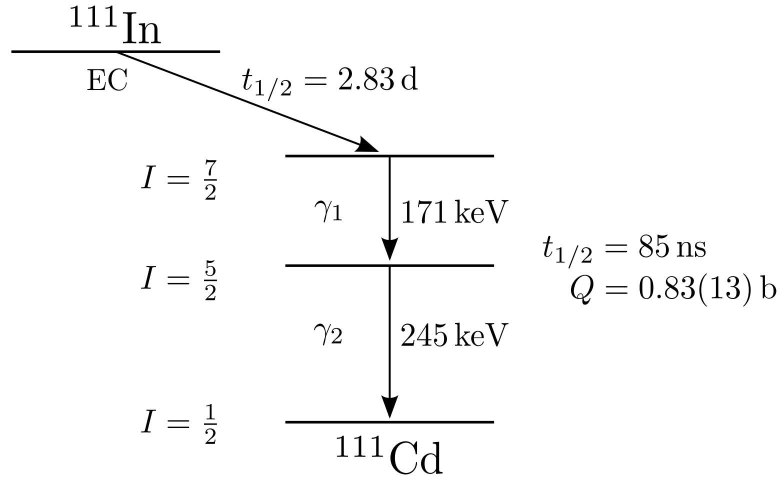

Fig. 3.7: ^{111}In decays via electron capture to an excited state of ^{111}Cd with a nuclear spin of $I_i = 7/2$. By the emission of two γ-rays with an energy of 171 keV and 245 keV via an intermediate state with a nuclear spin of $I = 5/2$ the nucleus proceeds to the ground state $I_f = 1/2$. The quadrupole moment of the intermediate state is $Q = 0.83(13)$ b.

4. Sample preparation

4.1 Ion implantation

The implantation of radioactive probe atoms is carried out at the Bonn Isotope Seperator. The ^{111}In probes are provided in a $^{111}InCl_3$-solution, which is commercially available from Covidien [1]. After vaporising the solution, the gas atoms are ionized and accelerated by an electric field. By deflecting the ion beam in a magnetic field a separation of different masses is achieved and only the desired isotope is implanted into the sample. ^{111}In decays to ^{111}Cd. The masses of both isotopes are only slightly different. Hence, taking the finite mass resolution of the seperator and life time of ^{111}In into account, a small amount of ^{111}Cd is implanted into the sample as well. To ensure a homogeneous distribution of implanted ions, the ion beam is sweeped over the sample. By varying the acceleration voltage implantation energies up to 160 keV are available. The implantation fluence is about $(10^{11} - 10^{12})$ ions/cm^2.

Since the investigated samples are monocrystalline, channeling of the accelerated ions can occur during the implantation. To prevent single ions from reaching far into the crystal, the samples are tilted by an angle of 7° with respect to the ion beam direction. According to former studies in our group, no channeling effects occur with this configuration.

In order to assure that the implanted indium probes are inside the silicon doped layer, the implantation profile is calculated with the simulation program *Stopping and Range of Ions in Matter (SRIM 2011)* [19]. The implantation depth depends on the energy and mass of the ions and the sample material. Figure 4.1 shows the result for doped GaN with a silicon percentage of 0.01 %. Given an atomic density in GaN of 8.79×10^{22} atoms/cm^3 [8], this corresponds to the highest available silicon concentration of 9.2×10^{18} atoms/cm^3 (see Table 2.2). The red line is a Gaussian distribution fitted to the data. For the calculation, the implantation energy was set to 160 keV and the inclination angle to 7°. The mean implantation depth is simulated to 399 Å, the full width at half maximum (FWHM) of the implantation profile to 158 Å and the maximum implantation depth to 1163 Å. In comparison to undoped GaN no difference in these parameters can be observed. Thus, the

[1] Covidien Deutschland GmbH, Gewerbepark 1, 93333 Neustadt a.d.Donau

influence of the silicon doping on the implantation profile can be neglected in this study. By comparing the maximum implantation depth with the thickness of the doped layer of 900 – 970 nm (see Table 2.2) one can see that the indium probes do not reach the GaN buffer layer beneath the silicon doped layer. It is worth mentioning that *SRIM* only considers amorphous materials so that channeling is not taken into account in the calculations. Nevertheless, the calculation results are reasonable, because channeling is avoided by choosing an inclination angle of 7°. Therefore, all samples are implanted with an implantation energy of 160 keV.

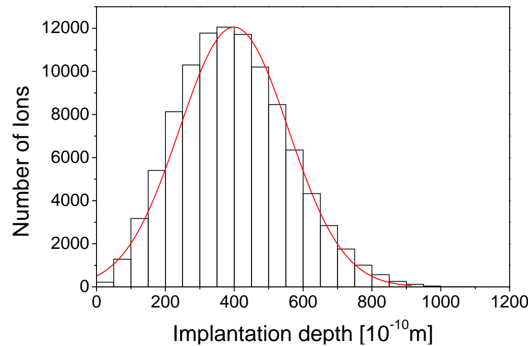

Fig. 4.1: Plot of the implantation profile of ^{111}In into GaN-Si with a silicon concentration of 0.01 % at an energy of 160 keV and an inclination angle of 7°. The red line is a Gaussian distribution fitted to the data. The mean implantation depth is simulated to 399 Å, the full width at half maximum to 158 Å and the maximal implantation depth to 1163 Å.

4.2 Annealing of implantation damage

Ion implantation is a very destructive method of introducing probe atoms into a sample. During the process of ion stopping, their energy is transferred to electrons and lattice atoms of the crystal. The energy of the accelerated ions is several orders of magnitude higher than the bond energy of the lattice atoms, which is 8.92 eV/atom [1] in GaN. Thus, lattice atoms are dislocated and lattice defects including interstitials and vacancies are created. Furthermore, the implanted ions are not well integrated into the crystal lattice and located on interstitial and substitutional lattice sites. When thermal energy is added to the system, the lattice atoms rearrange to a position of thermal equilibrium and the implantation damage is annealed. Therefore, the samples have to be tempered at high temperatures.

Due to the high melting point of group-III nitrides, high temperatures are required for recovering the lattice structure in GaN films. All samples for this study are tempered in a rapid thermal annealing apparatus (RTA). The RTA is described in

detail in the diploma thesis of Marx [20], so only a short description is given here. The sample is placed between two graphite stripes, which are connected to copper electrodes. A voltage between the electrodes leads to a current running through the graphite stripes, which eventually heats them up due to their electrical resistance. The point of highest temperature is exactly at the position of the sample. The temperature is measured by a thermocouple beneath the sample. The heating power is chosen such that temperatures up to 1400 K are reached within a few seconds. The tempering can be done under vacuum conditions or a nitrogen atmosphere with an adjustable gas flow.

According to the PhD thesis of Penner [21], the best annealing conditions for GaN are achieved when tempering under a nitrogen atmosphere and by means of a proximity cap. The proximity cap is another GaN film which is put on top of the sample. Due to the high vapour pressure nitrogen would otherwise diffuse out of the sample.

4.3 PAC furnace

Measurements at elevated temperatures are taken in a furnace which is especially designed for performing temperature-dependent PAC-measurements. Comprehensive information about it can be found in the diploma thesis of Arenz [22]. Therefore, only a short description of the furnace is given here.
The furnace is connected to a vacuum pump and a nitrogen supply. It can be placed in the middle of the four detectors with a distance of approximately 15 mm between the sample and each detector. In order to provide a minimal absorption in the furnace material, the sheathing of the furnace is 0.3 mm thick at the level of the detectors. Inside the furnace, the sample is put in a holder made of macor or one made of quartz. The holder is inserted into a graphite heater, which is hollow and slit from bottom up to its cap. A current, which is provided by two electrodes, runs through the heater and due to its electrical resistance the temperature rises. Temperatures up to 1100 K and 1300 K are possible with the macor and quartz holder, respectively. In order to protect the detectors from these high temperatures, the sheathing and the electrodes are watercooled.
The temperature regulation is performed by a proportional-integral-derivative controller (PID). A detailed description of the PID-program can be found in the diploma theses of Steffens [23] and Cojocaru [24].

All measurements in this study are taken under vacuum conditions and temperatures do not exceed 900 K.

5. Measurements

In this chapter, the measurement results are presented and discussed. Since the perturbed angular correlation is observed by measuring the time between two γ-rays, first the time resolution of the detector systems is determined (Section 5.1). The annealing behaviour after ion implantation is investigated for an undoped and a doped GaN sample (Section 5.2). Measurements with different orientations are taken to determine the symmetry of the EFGs (Section 5.3). Further investigations on the influence of silicon doping on the hyperfine fields in GaN are carried out with the six available GaN films at room temperature (Section 5.4) and at elevated temperatures (Section 5.5).

5.1 Time resolution of the PAC spectrometer

For the purpose of measuring the time resolution of the PAC spectrometer a ^{60}Co calibration source is used. A prompt curve is measured by setting the energy windows of the SCAs for the time measurement to the same energy range as the start and stop signal. The time resolution is energy dependent and the energies of the γ-rays in the decay cascade of ^{111}In are 171 keV and 245 keV. Therefore, the energy range between 170 keV and 250 keV is chosen. In order to improve the accuracy of the measurement, the time calibration of the TAC is set to 0.08 ns/chn. In an ideal case, the shape of the measured signal is a sharp line. But due to a finite time resolution one observes a broadening of the signal which can be described by a Gaussian distribution. In Figure 5.1 the measured prompt curves for the LSO and Ba_2F systems are shown. A Gaussian distribution, which is shown as a red line, is fitted to the data. The full width at half maximum (FWHM) of the distribution gives the time resolution. The time resolution of the LSO system is measured to be 1.108(4) ns and of the Ba_2F system 0.807(3) ns. For this reason in all following measurements the time calibration of the TAC is set to 0.81(1) ns/chn.

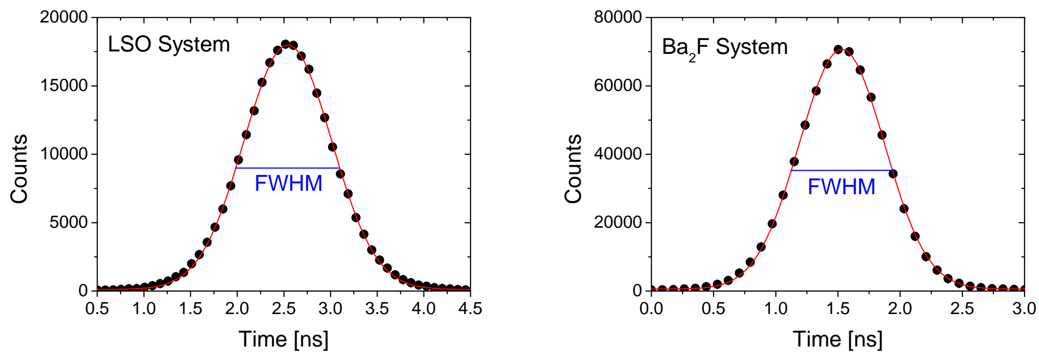

Fig. 5.1: The prompt curve is measured using a ^{60}Co calibration source, in order to determine the time resolution of the LSO (left) and Ba_2F (right) detector system. A Gaussian distribution, which is shown as a red line, is fitted to the data. The full width at half maximum (FWHM) of the distribution gives the time resolution, which is measured to be FWHM = 1.108(4) ns and FWHM = 0.807(3) ns for the LSO and Ba_2F system, respectively.

5.2 Annealing behaviour

In this section, the effect of the silicon concentration on the annealing behaviour after ion implantation in GaN is investigated.
Two samples are implanted with ^{111}In at an energy of 160 keV and a fluence of 10^{12} ions/cm^2. One sample is undoped GaN (GN5465) and the other one is doped GaN with a silicon concentration of 9.2×10^{18} atoms/cm^3 (GN4885). The process of lattice recovery is investigated by an isochronous annealing program using the RTA described in Section 4.2. At each annealing step, the samples are kept under a nitrogen flow of 75 l/h for two minutes at temperatures ranging from 600 K to 1400 K. In order to ensure that both samples are treated exactly under the same conditions, the films are tempered simultaneously and used as a proximity cap for each other. This prevents nitrogen from diffusing out of the samples. After each step, measurements are taken at room temperature with the c-axis of the crystal aligned at angle of 45° relative to the start detector.

5.2.1 Undoped GaN: GN5465

Figure 5.2 shows some recorded $R(t)$ spectra at selected temperatures for the undoped sample. Three different fractions are used to describe the curves fitted to the data, which are given as red lines. The annealing temperature dependence of the fit parameters is illustrated in Figure 5.3. All $R(t)$ spectra can be found in Figure B.1 and the fit parameters in Table A.1 in the appendix.
The first $R(t)$ spectrum is measured as implanted. As illustrated by the strong increase of $R(t)$ towards zero, the anisotropy shows a highly damped fraction f_p of 78(5) % with a high frequency of approximately 50 MHz. For this fraction polycrystalline properties are considered for least squares fitting. Besides that, a small monocrystalline fraction f_l of 22(2) % contributes to the anisotropy.
f_p rapidly decreases with increasing annealing temperature and disappears at a temperature of 1000 K. In contrast, f_l increases with every annealing step until 1200 K and declines towards higher temperatures. Beginning with a temperature of 800 K, a third monocrystalline fraction f_d appears in the spectrum, which reaches its maximum at 1300 K.
At 1400 K, the spectrum undergoes a visible change (see Figure 5.2). The anisotropy rises a little bit and remains constant at about 0.07. A large polycrystalline fraction f_c of 69.8(5) % with a neglectable slow frequency is needed in the fitting routine to describe the data.
The frequency $\nu_{Q,l}$ corresponding to f_l decreases with the annealing temperature. There is a huge change between as implanted and annealed at 800 K. Above that, the relative change of $\nu_{Q,l}$ is very small and a value of 5.08(5) MHz is reached.
$\nu_{Q,d}$ stays constant at about 9 MHz between 800 K and 1000 K and increases to approximately 16 MHz at higher temperatures.

The frequency of the polycrystalline fraction shows a strong temperature dependence and decreases from 49.9(9) MHz to 17.7(4) MHz.
The damping δ_l decreases constantly up to a temperature of 1300 K and reaches a minimum value of 18.0(5) %. At 1400 K, a slight increase can be observed. Except for the outlier at 1000 K, the damping δ_d declines with the annealing temperature from 46(1) % to 36(1) %. The damping of the polycrystalline fraction varies around a mean value of 75 %.

5.2.2 Highly doped GaN-Si: GN4885

Some recorded $R(t)$ spectra at selected annealing temperatures are shown in Figure 5.2. The annealing temperature dependence of the fit parameters is illustrated in Figure 5.3. Similar to the undoped sample, one polycrystalline fraction f_p and two monocrystalline fractions f_l and f_d are needed to describe the spectra. All $R(t)$ spectra can be found in Figure B.2 and the fit parameters in Table A.2 in the appendix.
After implantation, f_p contributes the most to the anisotropy with 75(3) %. f_p decreases with the annealing temperature and vanishes at 800 K. The monocrystalline fraction f_l steadily increases to a maximum value of 87(1) % at 1200 K. f_d first recognizable in the spectrum at 800 K declines with temperature. Higher temperatures lead to a strong decrease of f_l and an increase of f_d, accordingly. At a temperature of 1400 K, a polycrystalline fraction f_c of 31.2(3) % with a neglectable slow frequency is needed to describe the spectrum, like for the undoped GaN sample.
As shown in Figure 5.3, the frequency $\nu_{Q,l}$ changes rapidly after the first annealing step. Further annealing at higher temperatures leads only to a small change of $\nu_{Q,l}$. For example, between 1200 K and 1400 K $\nu_{Q,l}$ remains constant at about 7 MHz within error margins.
The frequency $\nu_{Q,d}$ shows a steep increase with temperature. Whereas the frequency of the polycrystalline fraction is not temperature dependent and stays constant at about 39 MHz.
A monotonic decline of the damping δ_l can be observed. The damping δ_d of the second fraction depends strongly on the annealing temperature and takes on values between 71(4) % and 431(19) %.

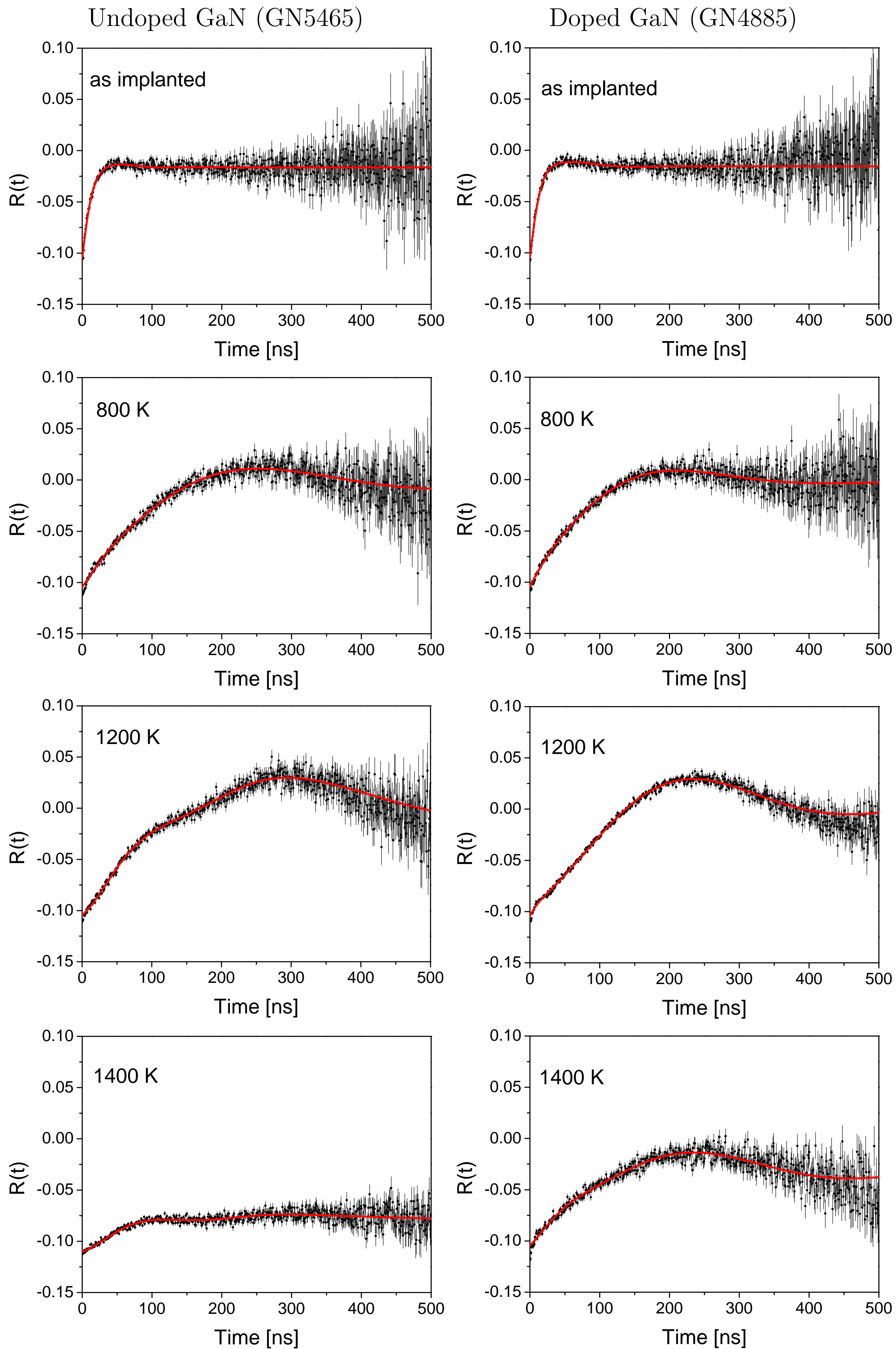

Fig. 5.2: Recorded R(t) spectra for undoped GaN (GN5465) and Si-doped GaN (GN4885) with a silicon concentration of 9.2×10^{18} atoms/cm^3 after selected annealing temperatures. The red line is the fit to the experimental data.

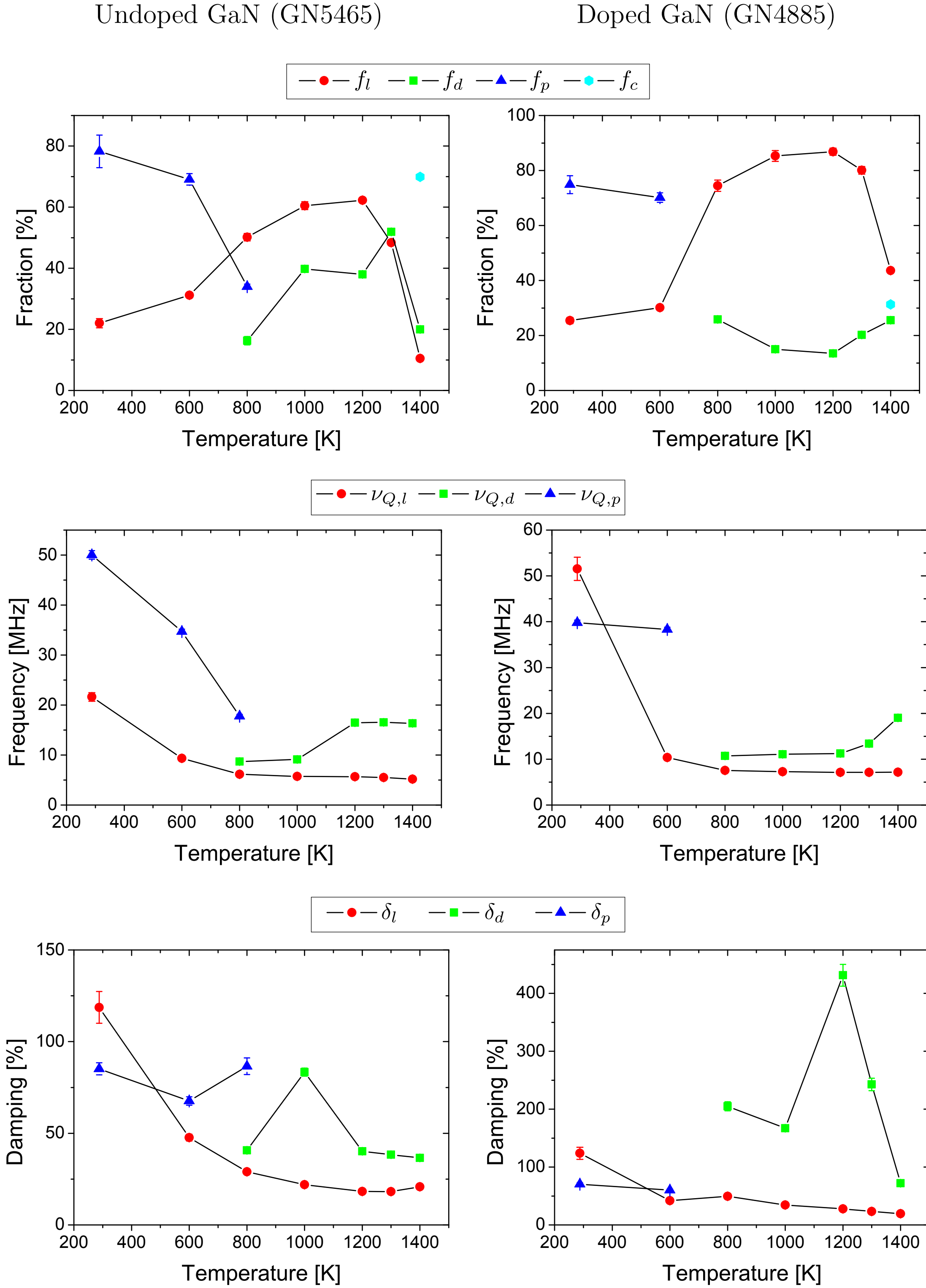

Fig. 5.3: Plots of the fit parameters for undoped GaN (GN5465) and doped GaN (GN4885) in dependence of the annealing temperature. Lines are drawn to guide the eye.

5.2.3 Discussion

First, the general annealing behaviour is discussed.
After implantation, the crystal lattice is heavily damaged, as expected, and most of the probe atoms are not located on substitutional sites. Thus, each probe atom is subjected to a different EFG. These EFGs strongly differ in magnitude and orientation in space. The resulting $R(t)$ spectrum is similar to a spectrum measured in a polycrystalline sample so that a polycrystalline fraction f_p is used in the fitting routine. The corresponding frequency $\nu_{Q,p}$ describes the mean EFG, which the probes are subjected to, whereas the corresponding damping δ_p is a measurement for the differences in magnitude of the EFGs. So, f_p is an indicator of the fraction of probe atoms, which are not well integrated into the lattice, and the amount of various defects still present in the crystal.
RBS/Channeling measurements showed that the majority of In-atoms replace Ga-atoms after annealing, as described in the PhD thesis of Lorenz [25]. At 1200 K, most probe atoms are described by f_l in the undoped GaN film, which shows a frequency of $\nu_{Q,l} = 5.57(5)$ MHz. The corresponding EFG of $V_{zz} = 0.9(1) \times 10^{15}$ V/cm^2 is typical for the EFG caused by the wurtzite lattice structure in GaN and will be referred to as the lattice EFG. K. Lorenz measured it to be $1.0(2) \times 10^{15}$ V/cm^2, which is in agreement within error margins. Thus, f_l can be identified with probe atoms, which are located in an undisturbed electronic environment. Defects on distant lattice sites cause small fluctuations of the EFG, which result in the damping δ_l. Therefore, f_l and δ_l are indicators of the crystal quality achieved through annealing. In the further course f_l is referred to as the lattice fraction.
As expected, f_p decreases and f_l increases with rising temperature, because the thermal energy added to the crystal initializes the lattice recovery and the probe atoms start to occupy substitutional lattice sites. The improvement of the crystal quality with each annealing step is illustrated by the steady decrease of δ_l and increase of f_l up to 1200 K.
The nature of the second fraction f_d is not known. Former studies by Keßler et al. [3] led to the assumption that nitrogen vacancies, which are trapped by probe atoms on the nearest N-site in c-direction, are responsible for f_d. The symmetry of the resulting EFG is in agreement with the results of Section 5.3. Furthermore, recent calculations by Laaksonen et al. [26] show that nitrogen vacancies are indeed the major point defect in GaN.
After annealing at 1300 K, both sample surfaces became slight milky. Investigating the films with a microscope revealed that the surfaces started to degrade and little droplets formed during the annealing process. This is unexpected, because a proximity cap was used. In Figure 5.4 pictures taken at a magnifaction of 100 are shown. It is likely that nitrogen atoms diffused out of the sample, so that the remaining droplets are liquid gallium. With the nitrogen atoms diffusing out, f_d increases and the fraction of probe atoms in an undisturbed lattice environment diminishes. This verifies the assumption of nitrogen vacancies causing f_d. Conse-

quently, f_d is referred to as the defect fraction.
The $R(t)$ spectra at 1400 K (Figure 5.2) are typical for measuring with ^{111}In in a liquid sample. Due to the thermal motion of the Ga-atoms inside the liquid huge EFGs are present, which are fast fluctuating in magnitude and orientation in space. So, when averaging over time, the EFG vanishes and the unperturbed angular correlation of the decay cascade with no time dependent modulation is observed. The probe atoms inside the liquid are described by a polycrystalline fraction f_c with no frequency, which acts like a constant shift of the anisotropy.

In the following, the influence of silicon doping on the annealing behaviour is discussed.
For comparison, the development of the crystal quality of the un- and doped sample is illustrated in Figure 5.5 on the basis of the fraction f_l and the damping δ_l. The values of f_l and δ_l are summarized in Table 5.1. As can be seen in Figure 5.5, f_l reaches a maximum value of 62.1(8) % in the undoped sample, whereas in the doped sample the highest value of f_l is measured to be 87(1) %. So, due to silicon doping more probes are integrated into an undisturbed lattice environment with no defect in the nearest neighbourhood. The further investigation of the influence of the silicon concentration on the fraction f_l will be part of Section 5.4.
The lower damping δ_l in undoped GaN indicates a smaller number of defects on distant lattice sites than in doped GaN. Silicon occupies Ga-sites in GaN [27]. If a substantial amount of probe atoms is located on lattice sites with a silicon atom in the vicinity, the damping δ_l will be increased. Given the silicon concentration of the doped sample, this can give an explanation for the higher damping δ_l.
From these measuremtents one can conclude that the best results are achieved after annealing at 1200 K independently of the silicon concentration.
In the doped sample the lattice frequency $\nu_{Q,l}$ is measured to be 7.02(7) MHz after annealing at 1200 K while in pure GaN $\nu_{Q,l}$ is 5.57(5) MHz. So, silicon doping shows a strong influence on the EFG and the further discussion will be part of Section 5.4.
An interesting behaviour can be observed for the temperature range above 1200 K. As discussed before, the sample surfaces degrade and the number of probe atoms with a nitrogen vacancy on the nearest lattice site increases. In the undoped sample this fraction prevails the fraction of probes in an undisturbed lattice environment. In contrast, in the doped sample there is in increase of nitrogen vacancies but yet most of the probes are in an undisturbed lattice environment, even at 1400 K. Furthermore, the fraction of probes inside the liquid gallium is about 30 % larger in the undoped than in the doped sample. This leads to the conclusion that doping with silicon prevents nitrogen from diffusing out of the sample and makes GaN films more insensitive to high temperatures.
A possible explanation, why the out diffusion of nitrogen is suppressed in the doped sample, is the formation of Si-N bonds. Katsikini et al. [28] report on

the formation of Si-N after high-dose Si implantation into GaN with a fluence of 1×10^{18} ions/cm^2. Although the silicon concentration in the sample investigated here is lower, the formation of Si-N can still be possible. Furthermore, Romano et al. [29] report on the growth rate of Si-N being three times higher, when the temperature is increased from 1073 K to 1353 K.
In summary, the best results are achieved after annealing at 1200 K for the un- and doped GaN sample. The fraction of probes integrated into an undisturbed lattice environment is significantly higher in doped than in undoped GaN. Furthermore, the incorporation of silicon makes GaN films more stable at high temperatures and prevents nitrogen from diffusing out.

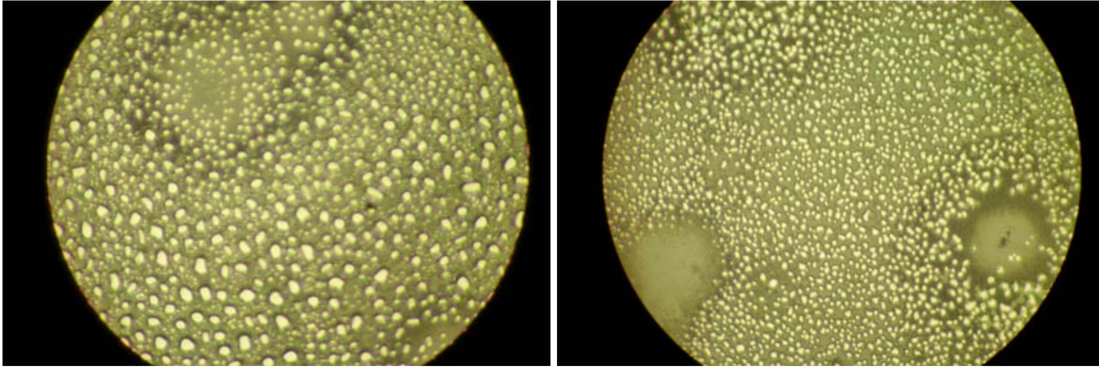

Fig. 5.4: Pictures of the degraded sample surface after annealing at 1400 K taken at a magnification of 100 for undoped GaN (left) and silicon doped GaN (right). It is likely that nitrogen diffused out of the sample, so that the droplets are liquid gallium.

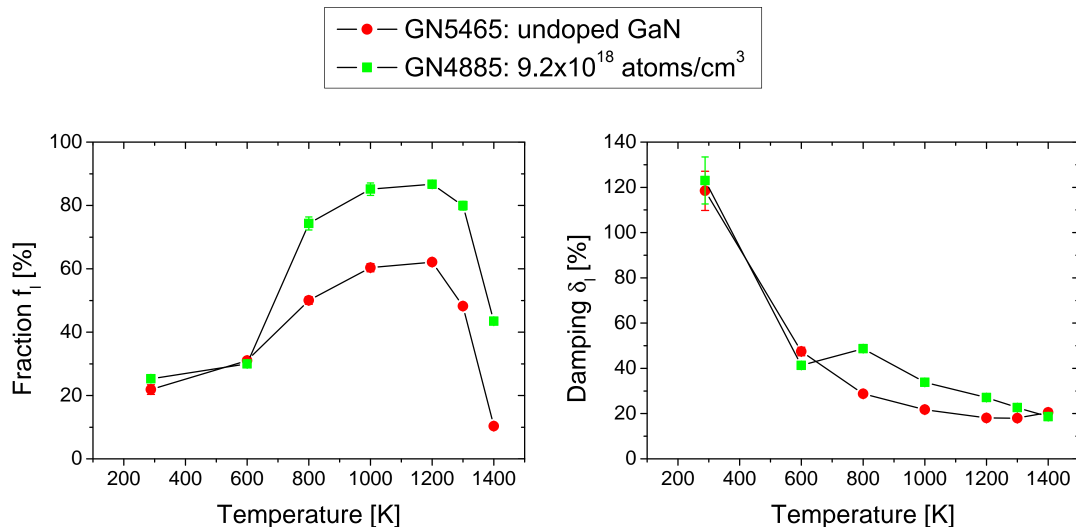

Fig. 5.5: For comparison, the lattice fraction f_l and damping δ_l in dependence of the annealing temperature are shown for doped and undoped GaN.

	f_l [%]		δ_d [%]	
Temperature [K]	Undoped GaN	Doped GaN	Undoped GaN	Doped GaN
as implanted	22(2)	25(1)	118(9)	123(10)
600	31.0(8)	30.0(7)	47(2)	41(2)
800	50(1)	74(2)	28.8(9)	48.7(8)
1000	60(1)	85(2)	21.7(6)	33.8(3)
1200	62.1(8)	87(1)	18.1(5)	27.1(2)
1300	48.2(4)	80(1)	18.0(5)	22.7(3)
1400	10.4(3)	43.5(7)	20(1)	18.6(7)

Tab. 5.1: Fit results for the fraction f_l of probes in an undisturbed lattice environment and the corresponding damping δ_l in dependence of the annealing temperature.

5.3 Determination of the symmetry of the electric field gradient

Orientation measurements are taken with the c-axis of the crystal pointing to the start detector for undoped GaN (GN5465) and doped GaN with a concentration of 9.2×10^{18} atoms/cm^3 (GN4885) after annealing at 1200 K. The recorded $R(t)$ spectra are shown in Figure 5.6.
In the case of the doped sample, the spectrum is shifted a little bit to higher values. The shift is due to different coincidence count rates of the detector combinations. Usually, twelve detector combinations contribute to the calculation of $R(t)$. When averaging over the coincidence count rates of the 180° and 90° detector combinations (see Eq. 3.27), differences between the count rates cancel each other, because each of the four detectors measures both the start and the stop signal. In contrast, for the orientation measurement two detectors measure the start signal and the other two the stop signal. Therefore, differences between the count rates are not corrected and a constant shift of $R(t)$ may occur. To account for that an additive constant of 0.02 is used in the fitting routine.
The spectra of both samples can be fitted with the same hyperfine parameters within error margins as for the 45° orientation, only corrected for the different angle. Hence, in both samples the two fractions f_l and f_d are caused by an EFG tensor whose symmetry is parallel to the c-axis of the crystal lattice. No influence of silicon doping on the symmetry of the EFGs is observed. The symmetry of the EFG causing the lattice fraction can be expected due to the wurtzite structure (see Section 2.1). The symmetry of the EFG causing the defect fractions agrees with the assumption that the defect is located on the N-site in c-direction (see Section 5.2).

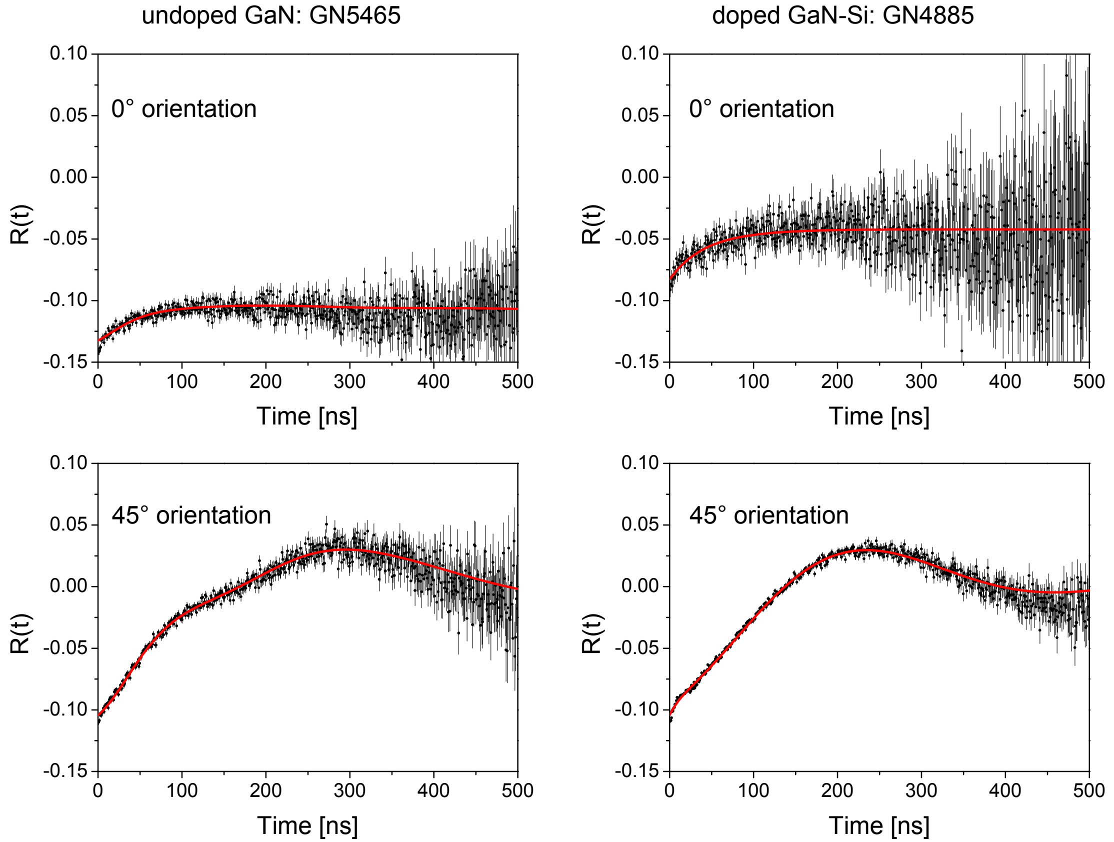

Fig. 5.6: Orientation measurements with the c-axis pointing to the start detector for the undoped GaN sample GN5465 (left) and the highly doped GaN-Si GN4885 with a silicon concentration of 9.2×10^{18} atoms/cm^3 (right) after annealing at 1200 K. The red line is the fit to the experimental data. From the measurements one can conclude that both fractions f_l and f_d are caused by an EFG tensor whose symmetry is parallel to the c-axis of the crystal lattice.

5.4 Influence of the silicon concentration on the hyperfine fields at room temperature

The influence of the silicon concentration on the hyperfine fields in doped GaN is investigated for six samples. One sample is undoped GaN, used as a reference, and the other five samples are silicon doped GaN with different concentrations ranging from 2×10^{17} atoms/cm^3 to 9.2×10^{18} atoms/cm^3. All samples are implanted with ^{111}In at an energy of 160 keV and an angle of 7°. After annealing at 1200 K, measurements at room temperature are taken using the standard setup, similar to Section 5.2.

5.4.1 Results

The $R(t)$ spectra are shown in Figure 5.7. The fits to the data consist of the two fractions f_l and f_d, similar to the measurements in Section 5.2.
From orientation measurements it is known that the two fractions originate from EFGs with a symmetry parallel to the c-axis of the crystals (see Section 5.3). The dependence of the silicon concentration on the hyperfine parameters is demonstrated in Figure 5.8. The measurements can be found in Table 5.4.1.

Independent of the silicon concentration, f_l is the dominant fraction causing the oscillation of the anisotropy with a low frequency. f_l increases with the concentration from 66(2) % for pure GaN to 84(1) % for a concentration of 9.2×10^{18} atoms/cm^3. For concentrations below 2×10^{18} atoms/cm^3 the relative increase of f_l is very strong. The frequency $\nu_{Q,l}$ changes little from 5.82(6) MHz for pure GaN to 6.05(6) MHz for 1.1×10^{18} atoms/cm^3 while in the two highest doped samples a huge increase of $\nu_{Q,l}$ to about 7 MHz is observed. The damping δ_l declines from 17.0(7) % for undoped GaN to 15.3(3) % for the lowest concentration of 2×10^{17} atoms/cm^3. Subsequent to that δ_l increases continuously to 23.9(3) % for 9.2×10^{18} atoms/cm^3.
f_d describes the steep slope in the first nanoseconds of the spectrum. Since $f_d = 1 - f_l$, the value of f_d decreases with the concentration. The corresponding frequency $\nu_{Q,d}$ fluctuates around a mean value of about 12(3) MHz for low concentrations and increases to 27(2) MHz for the highest concentration. As can be seen in the $R(t)$ spectra, f_d is highly damped. Especially for the two highest concentrations δ_d takes on values in the order 250 % and a correlation between δ_d and $\nu_{Q,d}$ can be observed in the fitting routine. Therefore, the influence of the silicon concentration on the corresponding EFG cannot be inferred from these measurements and only the fraction f_d is considered in the following discussion.

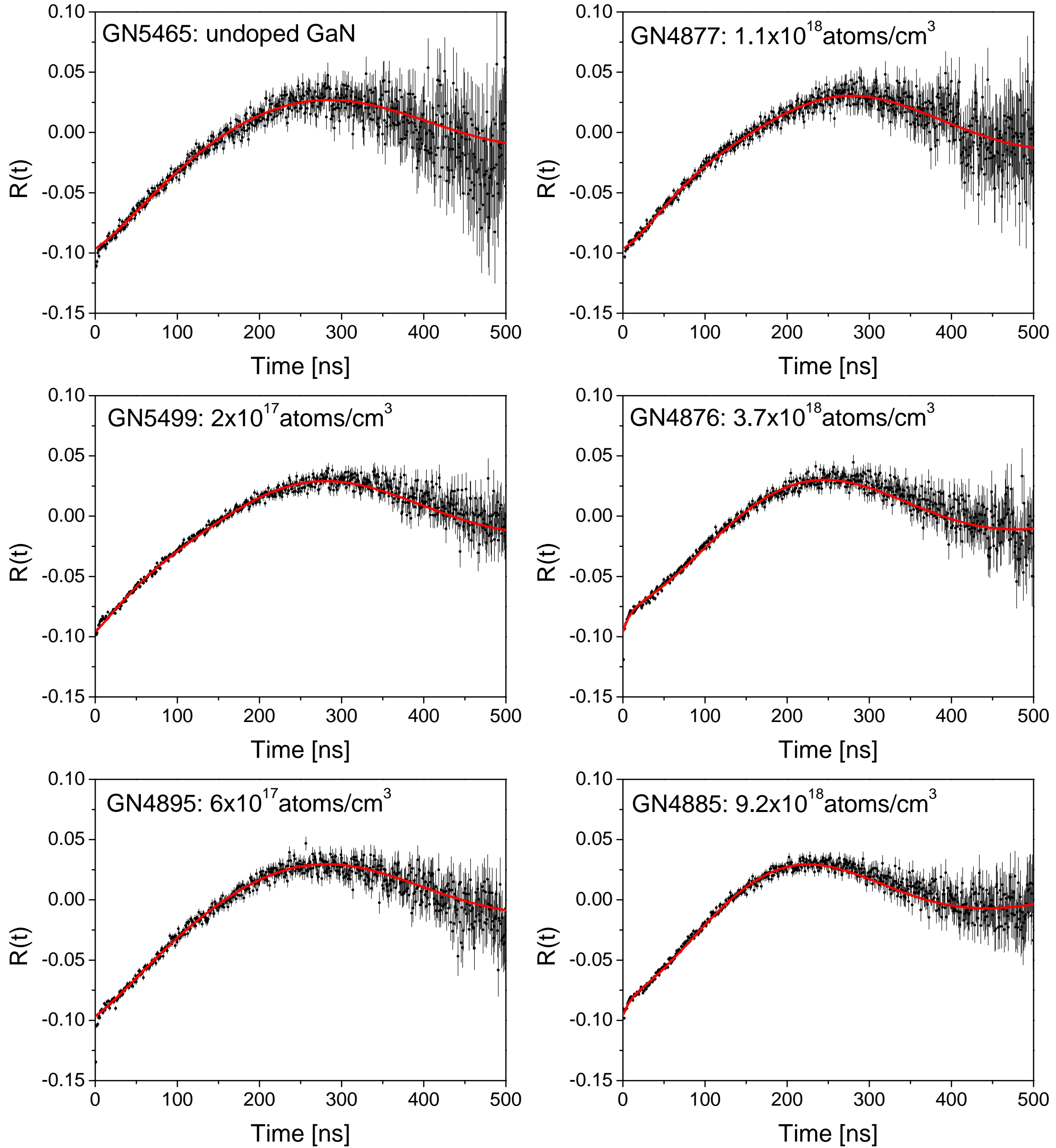

Fig. 5.7: $R(t)$ spectra measured at room temperature after annealing at 1200 K for different silicon concentrations. The red line is the fit to the experimental data.

5.4.2 Discussion

As illustrated in Figure 5.8, a higher concentration results in a higher fraction f_l of probe atoms replacing Ga-atoms in an undisturbed electronic environment. In Section 5.2, it was discussed that nitrogen vacancies, which are trapped by In probe atoms, cause the defect fraction f_d. A possible explanation for the increase of f_l and decline of f_d with the concentration is that the Si-atoms are a

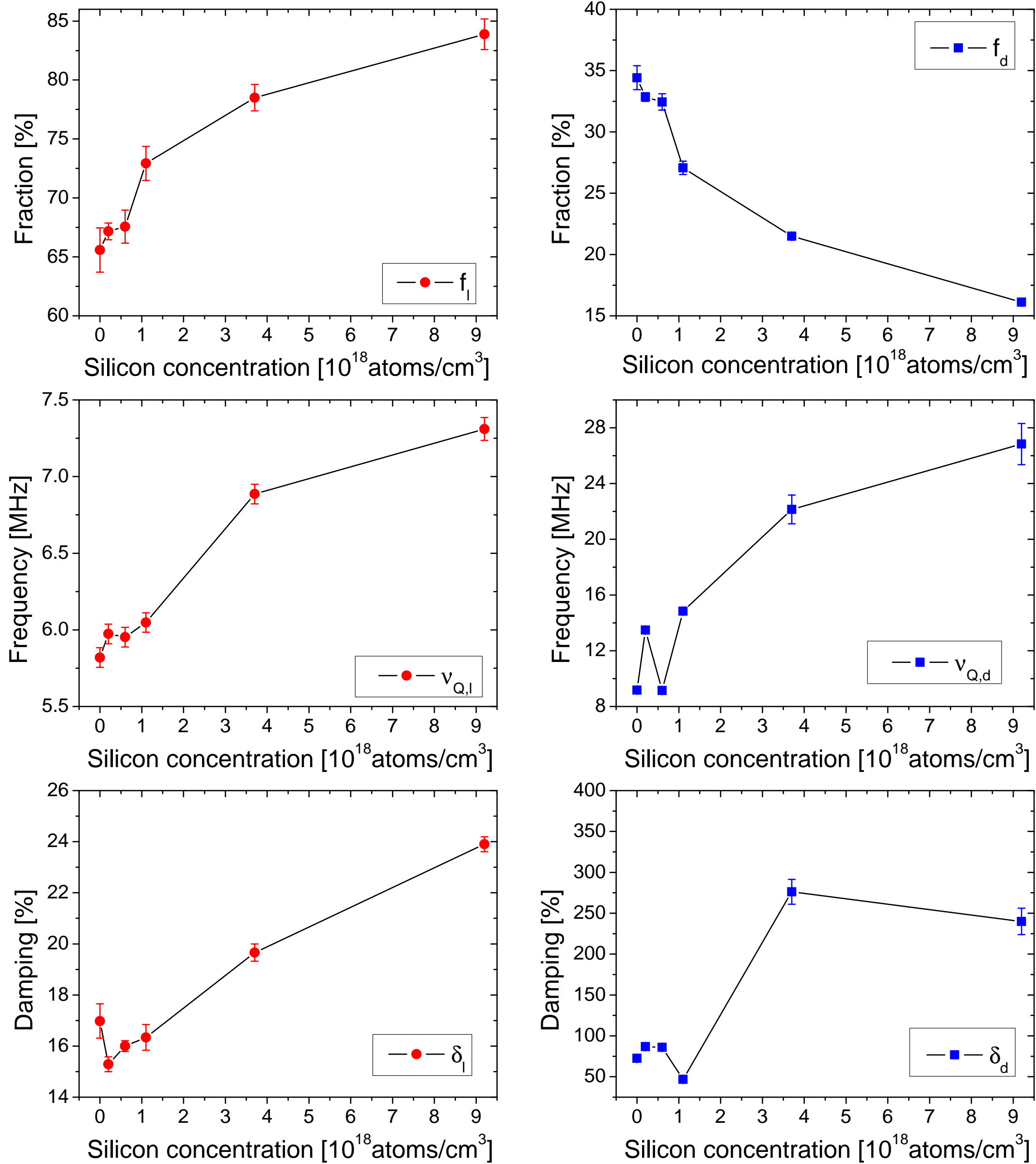

Fig. 5.8: Plots of the fit parameters in dependence of the silicon concentration measured at room temperature after annealing at 1200 K.

competing trap for nitrogen vacancies. Si-atoms occupy Ga-sites and are positively charged, because they act as donors [5]. Laaksonen et al. [26] report that nitrogen vacancies are negatively charged. So, an attractive interaction between Si-atoms and nitrogen vacancies occurs.
The observed increase of f_l and reduction of f_d is also in agreement with the results of Ruvimov et al. [30]. They report on an improved layer quality after doping with silicon to a concentration of 3×10^{18} atoms/cm^3 due to a reduction

Silicon concentration [$\times 10^{18}$ atoms/cm^3]	0	0.2	0.6	1.1	3.7	9.2
f_l [%]	65(1)	67.2(7)	68(1)	73(1)	79(1)	84(1)
$\nu_{Q,l}$ [MHz]	5.82(6)	5.97(6)	5.95(6)	6.05(6)	6.89(6)	7.31(7)
δ_l [%]	17.0(7)	15.3(3)	16.0(2)	16.3(5)	19.7(3)	23.9(3)
f_d [%]	34(1)	32.8(4)	32.4(7)	27.1(5)	21.5(3)	16.1(3)
$\nu_{Q,d}$ [MHz]	9.2(1)	13.5(1)	9.1(1)	14.8(2)	22(1)	27(1)
δ_d [%]	73(3)	87(2)	86(3)	47(2)	276(15)	240(16)

Tab. 5.2: Fit parameters of the $R(t)$ spectra measured at room temperature after annealing at 1200 K for varying silicon concentration.

of the dislocation density in the crystal. A lower dislocation density should also result in a reduction of the damping δ_l, which is consistent with the experimental results for δ_l up to a concentration of 1.1×10^{18} atoms/cm^3. However, the decrease of δ_l is only about 2 % from 17.0(7) % to 15.3(3) %.
The increase of δ_l for concentrations above 1.1×10^{18} atoms/cm^3 indicates a higher number of defects on distant lattice sites. This can be expected, because the probability that silicon atoms are located in the neighbourhood of indium probes is enhanced with increasing silicon concentration and the silicon atoms can be considered as point defects in the GaN lattice.
Cremades et al. [31] found the lattice constants a to increase and c to decrease with the silicon concentration, as shown in Figure 5.9. Since f_l rises with the concentration, it can be concluded that the change of the lattice constants facilitates the integration of In-atoms into an undisturbed lattice environment.

The increase of the lattice EFG with increasing concentration, especially for the two highest doped samples, is difficult to explain. For example, for the highest concentration V_{zz} is measured to be $1.2(2) \times 10^{15}$ V/cm^2 compared to $0.9(1) \times 10^{15}$ V/cm^2 for undoped GaN.
In the following, two possible scenarios are considered. While in the first scenario a change of the lattice constants, in the second an increased free charge carrier concentration is taken into account.
The EFG is very sensitive to the lattice constants a and c and the u-parameter. Given the results of Cremades et al. mentioned above, the c/a ratio decreases with the concentration, as shown in Figure 5.10. Corti et al. [32] calculated the EFG on the Ga-site for fixed u-parameter and varying c/a ratio. Considering the absolute value of the EFG, because the γ-γ-angular correlation is insensitive to the sign of the EFG, they obtain an increase of the EFG with increasing c/a ratio, as depicted in Figure 5.10. Although they did not consider In on a Ga-site,

the general dependence of the EFG on the c/a ratio should not change, since In is isoelectronic to Ga. These results imply that the EFG should decrease with increasing silicon concentration. This is in contradiction to the experimental results of this study. Thus, the assumption of a fixed u-parameter can be wrong and the incorporation of silicon leads to a change of u. As Corti et al. point out, the EFG depends crucially on the u-parameter. For example, an uncertainty of 0.1 % on u results in an uncertainty of approximately 20 % on the EFG.
Furthermore, an increase of the charge carrier concentration can result in a higher EFG. Barfuß et al. [33] report that in the semiconductor tellurium the EFG increases with the charge carrier concentration when measuring with ^{111}In. Köhler et al. [34] concluded, by comparing the charge carrier concentration measured by Hall-effect and the silicon concentration measured by SIMS, that in GaN-Si all silicon atoms are ionized and have contributed with one extra electron to the charge carrier concentration. Unintentionally doped GaN shows an intrinsic n-type conductivity with a charge carrier concentration of about 1×10^{16} electrons/cm^3 [34], which is two orders of magnitude smaller than the silicon concentration in the doped samples investigated here. So, the free charge carrier concentration is essentially increased by silicon doping.
In summary, the incorporation of silicon leads to a stronger lattice EFG, especially for high silicon concentrations. This can be due to a change of the u-parameter and an increase of the charge carrier concentration. The defect fraction, associated with nitrogen vacancies trapped by In probe atoms, decreases with the silicon concentration. This is attributed to Si-atoms being a competing trap for nitrogen vacancies. Furthermore, for concentrations up to 1.1×10^{18} atoms/cm^3 a lower damping δ_l than for undoped GaN can be observed.

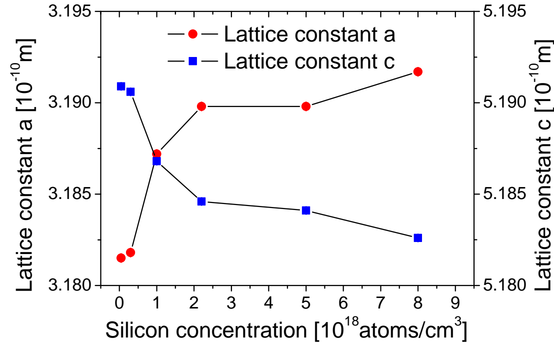

Fig. 5.9: Plot of the lattice constants a and c in dependence of the silicon concentration. Values were taken from Cremades et al. [31]. Lines are drawn to guide the eye.

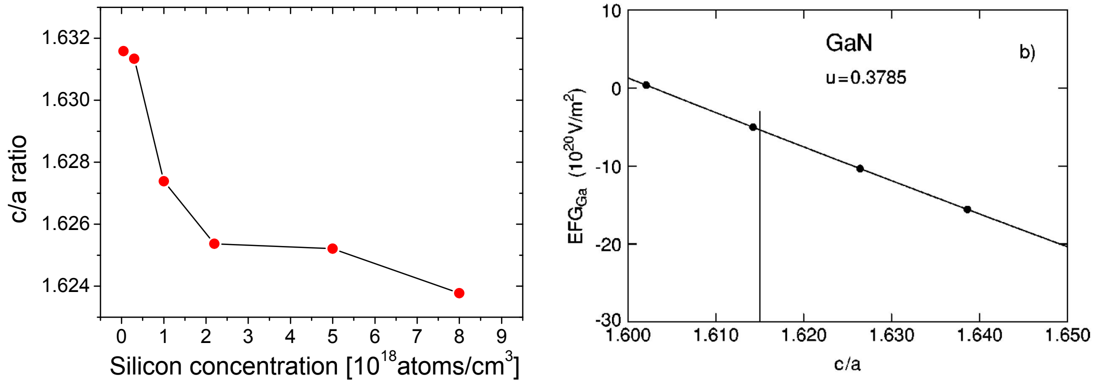

Fig. 5.10: Left: The c/a ratio in dependence of the silicon concentration. Values were taken from Cremades et al. [31]. Lines are drawn to guide the eye. Right: The EFG at the Ga site in dependence of the c/a ratio for fixed u-parameter. The graph was taken from Corti et al. [32].

5.5 Temperature dependent measurements

Measurements between room temperature and 900 K are taken using the PAC furnace (see Section 4.3), in order to investigate the influence of silicon doping on the temperature dependence of the hyperfine fields in GaN. The samples are implanted and annealed in the same way as before (see Section 5.4). For the measurements the standard setup is used (see Section 5.2). Due to absorption and scattering of the γ-rays in the furnace material the anisotropy $R(t)$ is reduced. In order to account for that, a multiplicative constant of 0.82 is used in the fitting routine. This is discussed in the diploma thesis of Ruske [17].

5.5.1 Results

In Figure 5.11 $R(t)$ spectra at selected temperatures are shown using the example of silicon concentrations of $1.1 \times 10^{18}\,\mathrm{cm}^{-3}$ (GN4877) and $9.2 \times 10^{18}\,\mathrm{cm}^{-3}$ (GN4885). The curves fitted to the data are described by the two fractions f_l and f_d similarly to former measurements (see Section 5.4). At room temperature, one can clearly recognize the two fractions for both samples. Between 400 K and 700 K, the $R(t)$ spectrum for GN4877 undergoes a visible change and f_l alone is sufficient to fit the data. In comparison, in the $R(t)$ spectra for GN4885 f_d is present up to 900 K, which is indicated by the steep slope in the first nanoseconds.
The fit parameters for all samples can be found in Tables A.3-A.8 and the $R(t)$ spectra are shown in Figures B.3 - B.8 in the appendix.
The effect of the concentration on the temperature dependence of f_l is depicted for four different concentrations in Figure 5.13.b. Independent of the concentration, f_l steadily increases up to 500 K and remains constant for higher temperatures. Since $f_d = 1 - f_l$, the value of f_d shows the opposite behaviour. However, silicon doping influences the maxium value of f_l. For undoped GaN and low concentrations of 6×10^{17} atoms/cm^3 and 1.1×10^{18} atoms/cm^3 the defect fraction f_d disappears completely above 500 K. f_l is therefore set to 100 % at higher temperatures.
In contrast, for the two highest concentrations, f_d is recognizable even at 900 K and f_l reaches a maximum value of only 85(2) % and 89(3) %. The same behaviour can be observed in the sample with the lowest silicon concentration of 2×10^{17} atoms/cm^3, where f_l does not exceed 92(2) %.
Since f_l is already large at room temperature for the two highest concentrations, it shows only a slow increase with temperature.

Throughout all samples the lattice frequency $\nu_{Q,l}$ increases with temperature. The temperature dependence of $\nu_{Q,l}$ is shown in Figure 5.13.a for all investigated samples. $\nu_{Q,l}$ changes little up to 400 K and steadily increases for higher temperatures, which is even visible in the $R(t)$ spectra (Figure 5.11). Above 500 K, the measuring points for all concentrations almost lie on parallel lines. Thereby, the

frequencies for low concentrations including undoped GaN agree well with each other within error margins.
At room temperature, $\nu_{Q,l}$ is approximately 6 MHz for un- and doped GaN with a concentration less than 2×10^{18} atoms/cm^3. However, in the two highest doped samples $\nu_{Q,l}$ is approximately 7 MHz. This difference of 1 MHz is significantly reduced to about 0.6 MHz at 900 K.
In Figure 5.13 the dependence of $\nu_{Q,l}$ on the silicon concentration is illustrated for selected temperatures. Up to 900 K an increase of $\nu_{Q,l}$ with the concentration can be observed.

The temperature dependence of the damping δ_l changes with the silicon doping, as depicted for selected concentrations in Figure 5.12.c. For un- and doped GaN with a concentration up to 1.1×10^{18} atoms/cm^3 δ_l strongly increases up to 350 K. Higher temperatures lead to a steady decline, so that δ_l becomes significantly smaller compared to at room temperature. In contrast, for the two highest doped samples δ_l shows a constant decline.
Considering temperatures above 400 K, δ_l is smaller in doped than in undoped GaN for concentrations up to 3.7×10^{18} atoms/cm^3. This is illustrated in Figure 5.13 where the dependence of δ_l on the concentration is shown for selected temperatures.

For the same reasons as in Section 5.4 the temperature dependence of the damping δ_d and frequency $\nu_{Q,d}$ of the defect fraction f_d, especially for the two highest concentrations, is not considered here.

Subsequent to the 900 K measurement the $R(t)$ spectrum is again recorded at room temperature to assure that the films were not damaged by the high temperatures. When fitting the experimental data, no deviations in the hyperfine parameters within error margins are observed relative to before the high temperature measurements (see Tables A.3-A.8 in the appendix). So, the observed temperature dependence of the hyperfine fields is reversable.

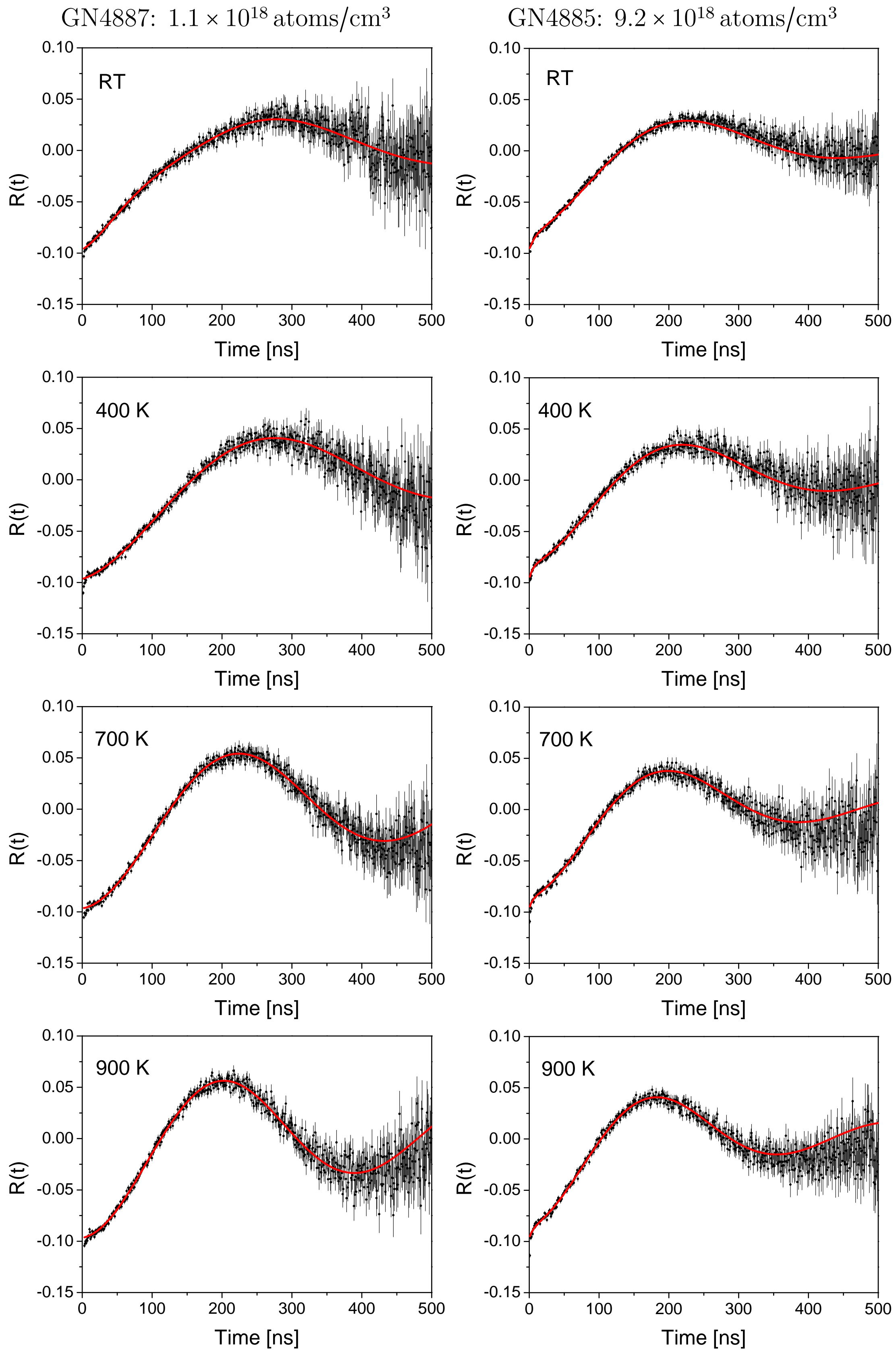

Fig. 5.11: Recorded R(t) spectra for two doped GaN samples with a silicon concentration of 1.1×10^{18} atoms/cm^3 (GN4877) and 9.2×10^{18} atoms/cm^3 (GN4885) at selected temperatures. One can clearly see the lattice and defect fraction at room temperature and 400 K in both samples, whereas at higher temperatures the defect fraction is only present in GN4885.

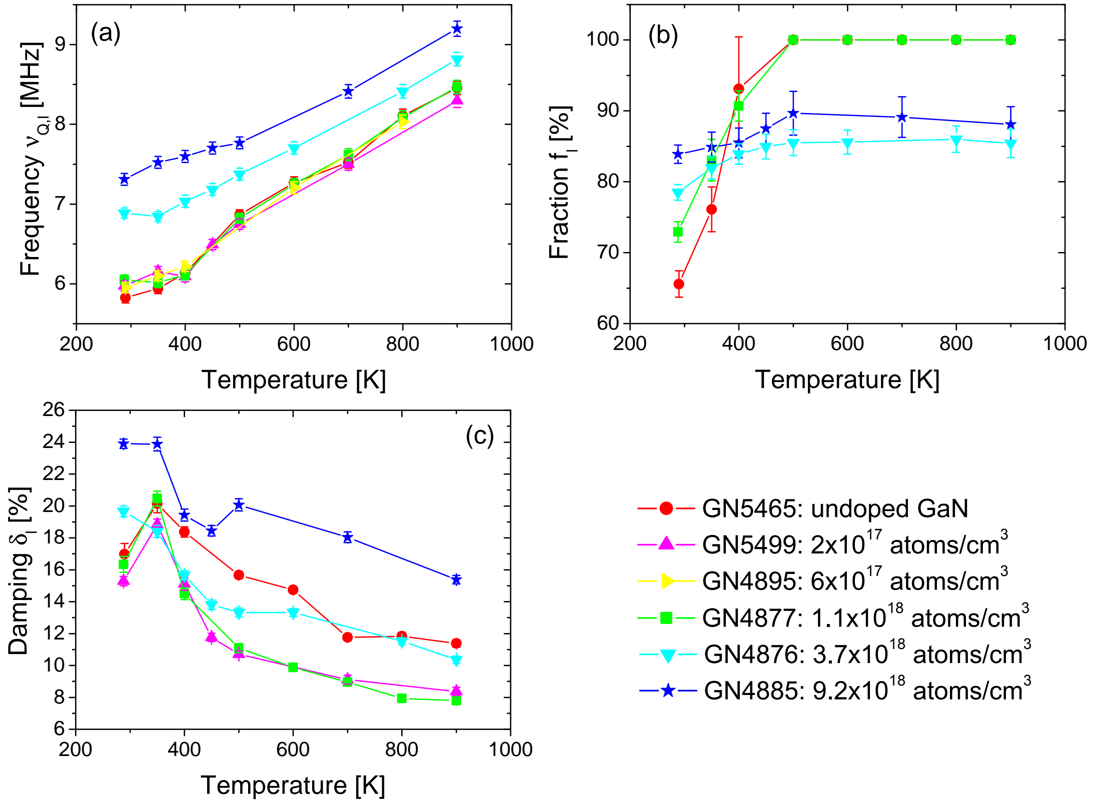

Fig. 5.12: The temperature dependence of the frequency $\nu_{Q,l}$ (a), the fraction f_l (b) and the damping δ_l (c) for selected silicon concentrations. Lines are drawn to guide the eye.

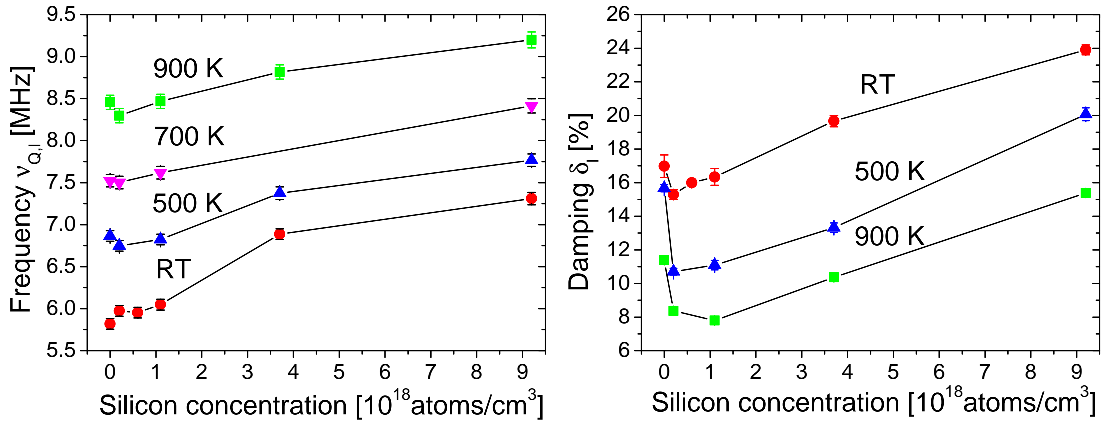

Fig. 5.13: The dependence of the frequency $\nu_{Q,l}$ (left) and damping δ_l (right) on the silicon concentration for selected temperatures. Lines are drawn to guide the eye.

5.5.2 Discussion

The lattice EFG increases with temperature independently of the silicon concentration. This was also observed by Ruske in his diploma thesis [17] for undoped GaN. A possible explanation for an increasing EFG is the thermal expansion of the lattice. Leszczynski et al. [35] found the thermal expansion coefficients for the lattice constants a and c to be different from each other and the resulting c/a ratio to decrease with temperature. However, theoretical calculations with a fixed u-parameter by Ruske show that the change of the c/a ratio is not sufficient to explain the huge increase of the EFG of about 30 %. He concludes that a temperature dependent change of the u-parameter causes the gain of the EFG.
The increasing EFG can also be caused by a higher charge carrier concentration. Götz et al. [5] found the charge carrier concentration in silicon doped GaN to increase with temperature. This also corresponds to the observation that the EFG rises with the silicon concentration at room temperature (see Section 5.4).
Christiansen et al. [36] report that the temperature dependence of the EFG in several non-cubic metals can be reproduced by the simple relation:

$$\nu_{Q,l}(T) = \nu_{Q,l}(0)(1 - BT^{3/2}). \tag{5.1}$$

Ruske assigned the same dependence to the EFG in GaN. His results are in good agreement with the assumed $T^{3/2}$-dependence and he obtains a value of $B = -1.75(1) \times 10^{-5}\,\mathrm{K}^{-3/2}$.
For a quantitive description of the influence of the silicon concentration on the temperature dependence of the EFG the relation 5.1 is fitted to the experimental data. In Figure 5.14 the frequency $\nu_{Q,l}$ is plotted versus $T^{3/2}$ using the example of a concentration of 9.2×10^{18} atoms/cm^3 (GN4885). The red line is the linear fit to the data. The results including χ^2 for all concentrations are summarized in Table 5.3. The significance of the fits is not very high, because only the range between room temperature and 900 K is considered and the number of measurements is relatively low. But the values for the slope B are of the same order as the result obtained by Ruske. For un- and doped GaN up to 1.1×10^{18} atoms/cm^3 no influence of the concentration on B can be observed within error margins. However, for the two highest concentrations one can see a significant decrease of B. This leads to the conclusion that silicon doping causes a less pronounced increase of the EFG with temperature. Ambacher [9] reports that the thermal expansion coefficient depends on many parameters, e.g. the defect concentration and free charge carrier concentration. Since the silicon atoms are extrinsic point defects and act as donors, an influence of the silicon concentration on the temperature dependence can be expected.
The influence of the concentration on $\nu_{Q,l}(0)$ cannot be inferred from the measurements in this study, because measurments below room temperature were not taken. Since $\nu_{Q,l}$ is essentially higher at room temperature for the two highest concentrations (see Figure 5.8), the fit also yields a higher $\nu_{Q,l}$ at $T = 0\,\mathrm{K}$.

For all concentrations the lowest damping δ_l is achieved at 900 K. This indicates a smaller number of defects on distant lattice sites than at room temperature. A possible explanation is a reduction of the lattice mismatch between substrate and GaN layer with increasing temperature due to different thermal expansion coefficients. This hypothesis is confirmed by Leszczynski et al. [35], who observed a reduction of the lattice mismatch with temperature. Ambacher [9] reports that the lattice mismatch induces residual stress, which can cause structural defects. So, when the samples are heated, the stress is reduced and with it the structural defects are annealed.
In Section 5.4 a lower damping δ_l than for undoped GaN was observed at room temperature for concentrations up to 1.1×10^{18} atoms/cm^3. However, the decrease in the damping was only about 2 % from 17.0(7) % to 15.3(3) %. In Figure 5.13 one can see that this reduction of δ_l is more pronounced at elevated temperatures. Furthermore, even for $3.7{\times}10^{18}$ atoms/cm^3 δ_l is lower than for undoped GaN.

Independent of the silicon concentration, the fraction of probes subjected to the lattice EFG increases with temperature. This increase was also observed in previous studies by Keßler et al. [37] in undoped GaN. They concluded that different bond energies of the defect to In and Cd lead to a reduction of the defect fraction with increasing temperature. As discussed in the last sections, it is likely that nitrogen vacancies, trapped by the probe atoms, are the origin of the defect fraction. At low temperatures, the thermal energy is not sufficient to break the bond between a nitrogen vacancy and a Cd-atom. So, probes in an undisturbed lattice environment and probes with a nitrogen vacancy in the nearest neighbourhood contribute to the $R(t)$ spectrum. At high temperatures, the bond is broken and nitrogen vacancies diffuse to the surface, because it is energetically more favorable. Thus, nitrogen vacancies near probe atoms are annihilated. The half life of the initial state of the decay cascade in ^{111}Cd is 120 ps. If a nitrogen vacancy is annihilated, before this state decayed, only the lattice EFG will be measured.
The reversibility of the temperature dependent effects leads to the assumption that nitrogen vacancies are stronger bonded to In than to Cd. Even at high temperatures nitrogen vacancies remain bonded to In-atoms, which have not decayed yet. When measurements are subsequently taken at room temperature, these In atoms decay to Cd and the defect fraction is observable again in the $R(t)$ spectrum.
For un- and doped GaN up to a concentration of 1.1×10^{18} atoms/cm^3 all probe atoms are subjected to the lattice EFG above 500 K. However, in the lowest doped sample the lattice fraction reaches a maximum value of only 92(2) %. This can be attributed to a not well annealed sample. For the two highest doped samples the maximum value of f_l is significantly lower and even at 900 K a substantial

fraction of probe atoms is subjected to an EFG caused by a nitrogen vacancy in the nearest neighbourhood. This indicates an increased binding energy between Cd-atom and nitrogen vacancy due to the high silicon concentration, although silicon atoms are a competing trap for nitrogen vacancies (see Section 5.4).

In summary, in highly silicon doped GaN the increase of the lattice EFG with temperature is less pronounced than in undoped GaN. The defect fraction, attributed to a nitrogen vacancy in the nearest neighbourhood, is stable up to 900 K for concentrations above 3.7×10^{18} atoms/cm^3. This indicates a higher binding energy between Cd-atom and nitrogen vacancy. Furthermore, the reduction of the damping, which was observed for low concentrations at room temperature (see Section 5.4), is more pronounced at elevated temperatures.

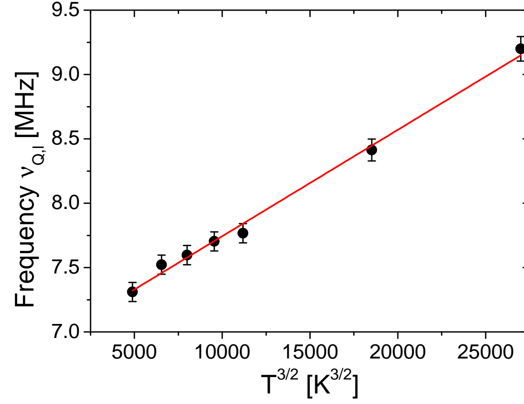

Fig. 5.14: The frequency $\nu_{Q,l}$ is plotted versus $T^{3/2}$ for a concentration of 9.2×10^{18} atoms/cm^3 (GN4885). T is the temperature. The red line is the linear fit to the data: $\nu_{Q,l}(T) = \nu_{Q,l}(0)(1 - BT^{3/2})$.

Silicon concentration [10^{18} atoms/cm^3]	$\nu_{Q,l}(0)$ [MHz]	B [10^{-5} K$^{-3/2}$]	χ^2
0	5.2(1)	-2.4(2)	0.973
0.2	5.41(9)	-2.0(1)	0.995
0.6	5.31(7)	-2.3(1)	0.991
1.1	5.3(1)	-2.3(1)	0.974
3.7	6.33(5)	-1.45(6)	0.990
9.2	6.92(4)	-1.20(4)	0.992

Tab. 5.3: Results for the linear fit of $\nu_{Q,l}(T) = \nu_{Q,l}(0)(1 - BT^{3/2})$ to the data for all concentrations.

6. Summary

The influence of silicon doping on the hyperfine fields in GaN films is investigated with the perturbed γ-γ-angular correlation method. Measurements on silicon doped GaN films with concentrations ranging from 2×10^{17} atoms/cm^3 to 9.2×10^{18} atoms/cm^3 are taken. An undoped GaN film is used as a reference sample. All samples are grown by Ambacher and Köhler using the same process to assure comparibility.

The investigation of the annealing behaviour shows that the best results are achieved after annealing at 1200 K. Tempering at 1400 K demonstrates that high silicon concentrations make GaN films more stable at high temperatures. This is attributed to the formation of Si-N bonds, which prevent nitrogen from diffusing out of the sample.

Measurements with different sample orientations show that the EFGs, which cause the two fractions f_l and f_d in the $R(t)$ spectra, have a symmetry parallel to the c-axis of the crystal. This agrees with the results of previous studies [25]. No influence of silicon doping on the symmetry is observed.

Measurements at room temperature for different silicon concentrations after annealing at 1200 K yield that the EFG, caused by the wurtzite lattice structure, increases with the silicon concentration. This can be due to a change of the u-parameter, caused by the incorporation of silicon atoms, or an increase of the charge carrier density. From temperature dependent measurements up to 900 K it is concluded that the increase of the EFG with temperature is less pronounced when doping with concentrations larger than 3.7×10^{18} atoms/cm^3.

Furthermore, compared to undoped GaN a lower damping is observed up to a concentration of 1.1×10^{18} atoms/cm^3 at room temperature. The results can be attributed to a reduced dislocation density, caused by the silicon doping [30]. This reduction of the damping is enhanced at higher temperatures. At 900 K, up to 3.7×10^{18} atoms/cm^3 a lower damping than for undoped GaN is measured.

Troughout all samples, a fraction of probe atoms subjected to a large EFG is observed in the $R(t)$ spectra. This fraction is attributed to a nitrogen vacancy, trapped by a probe atom on the nearest N-site in c-direction [3]. At room temperature, the fraction decreases with the silicon concentration. This leads to the assumption that Si-atoms are a competing trap for nitrogen vacancies. However, temperature measurements show that the binding energy between probe atom and nitrogen vacancy is increased due to silicon doping. For silicon concentrations larger than 3.7×10^{18} atoms/cm^3 the bond between probe atom

and nitrogen vacancy is measured to be stable up to 900 K while for lower concentrations the corresponding fraction disappears in the $R(t)$ spectra at 500 K.

7. Outlook

To further investigate the influence of the charge carrier concentration, GaN codoped with silicon and carbon should be considered for future measurements. Xie et al. [38] report that carbon acts as a compensator and reduces the free charger carrier concentration. Since only n-type GaN was investigated, p-type material should be taken into consideration, as well. The p-type conductivity of GaN is achieved by doping with magnesium.

While investigating the annealing behaviour (Section 5.2) a possible influence of the proximity cap material is observed. Figure 7.1 shows the $R(t)$ spectra measured in pure GaN after annealing at 1200 K with a pure GaN and a silicon doped GaN proximity cap. The silicon concentration is 9.2×10^{18} atoms/cm^3. Two monocrystalline fractions f_l and f_d contribute to the $R(t)$ spectrum, similar to other measurements (see Section 5.4). Regarding the cap material, the fractions and lattice frequencies are measured to be equal within error margins. But obviously, the defect frequency, which can be identified with the steep slope in the first 100 ns, is higher, when the silicon doped GaN proximity cap is used.

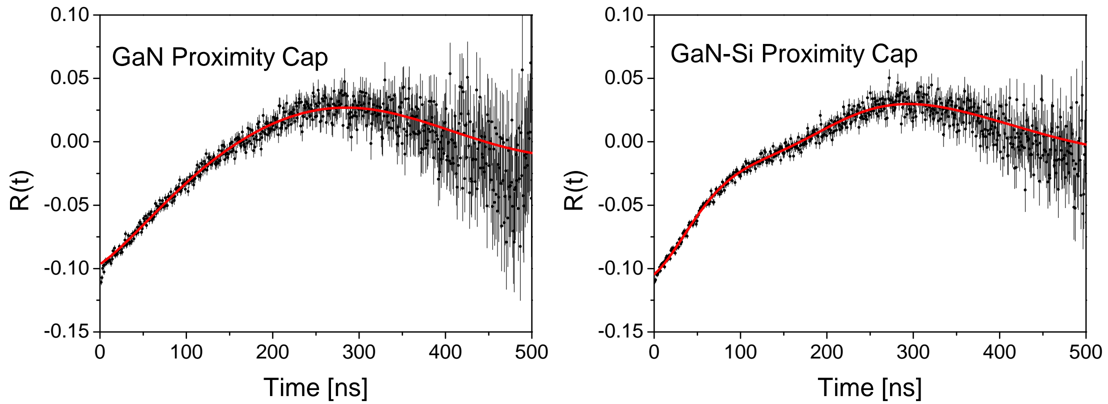

Fig. 7.1: The $R(t)$ spectrum of pure GaN (GN5465) measured after annealing at a temperature of 1200 K with a GaN proximity cap (left) and a GaN-Si proximity cap (right) with a silicon concentration of 9.2×10^{18} atoms/cm^3. When using the GaN-Si cap, the defect frequency, which is responsible for the steep slope in the beginning, is more pronounced.

Appendix

A. Tables

A.1 Annealing behaviour

Temperature [K]	f_l [%]	$\nu_{Q,l}$ [MHz]	δ_l [%]	f_d [%]	$\nu_{Q,d}$ [MHz]	δ_d [%]
as inplanted	22(2)	21.5(9)	118(9)	-	-	-
600	31.0(8)	9.3(1)	47(2)	-	-	-
800	50(1)	6.08(3)	28.8(9)	16(1)	8.6(2)	40(1)
1000	60(1)	5.66(5)	21.7(6)	39.6(4)	9.0(1)	83(2)
1200	62.1(8)	5.57(5)	18.1(5)	37.9(5)	16.4(1)	40(1)
1300	48.2(4)	5.41(5)	18.0(5)	51.8(5)	16.47(7)	38.1(6)
1400	10.4(3)	5.08(5)	20(1)	19.8(2)	16.3(2)	36(1)

Temperature [K]	f_p [%]	$\nu_{Q,p}$ [MHz]	δ_p [%]	f_c [%]
as inplanted	78(5)	49.9(9)	85(3)	-
600	68(2)	34.6(5)	67(2)	-
800	33.8(8)	17.7(4)	86(4)	-
1000	-	-	-	-
1200	-	-	-	-
1300	-	-	-	-
1400	-	-	-	69.8(5)

Tab. A.1: Fit parameters for the undoped sample GN5465 in dependence of the annealing temperature. f_l is the fraction of probes in an undisturbed lattice environment. $\nu_{Q,l}$ and δ_l are the corresponding frequency and damping. f_d is the fraction of probes with a point defect in the nearest neighbourhood. $\nu_{Q,d}$ and $\delta_{Q,d}$ are the corresponding frequency and damping, respectively. f_c is identifed with the fraction of probes in liquid gallium after annealing at 1400 K. The corresponding frequency $\nu_{Q,c}$ and damping δ_c are set to 0.

Temperature [K]	f_l [%]	$\nu_{Q,l}$ [MHz]	δ_l [%]	f_d [%]	$\nu_{Q,d}$ [MHz]	δ_d [%]
as inplanted	25(1)	51(3)	123(10)	-	-	-
600	30.0(7)	10.3(1)	41(2)	-	-	-
800	74(2)	7.46(7)	48.7(8)	25.7(7)	10.6(3)	204(7)
1000	85(2)	7.17(7)	33.8(3)	14.9(3)	11.0(1)	166(5)
1200	87(1)	7.02(7)	27.1(2)	13.3(2)	11.1(5)	430(19)
1300	80(1)	7.03(7)	22.7(3)	20.1(4)	13.3(5)	242(11)
1400	43.5(7)	7.08(7)	18.6(7)	25.4(4)	18.9(5)	71(4)

Temperature [K]	f_p [%]	$\nu_{Q,p}$ [MHz]	δ_p [%]	f_c [%]
as inplanted	75(3)	39.7(6)	70(2)	-
600	70(2)	38.2(5)	60(2)	-
800	-	-	-	-
1000	-	-	-	-
1200	-	-	-	-
1300	-	-	-	-
1400	-	-	-	31.2(3)

Tab. A.2: Fit parameters for the doped sample GN4885 in dependence of the annealing temperature. f_l is the fraction of probes in an undisturbed lattice environment. $\nu_{Q,l}$ and δ_l are the corresponding frequency and damping. f_d is the fraction of probes with a point defect in the nearest neighbourhood. $\nu_{Q,d}$ and $\delta_{Q,d}$ are the corresponding frequency and damping, respectively. f_c is identifed with the fraction of probes in liquid gallium after annealing at 1400 K. The corresponding frequency $\nu_{Q,c}$ and damping δ_c are set to 0.

A.2 Temperature dependent measurements

Temperature [K]	f_l [%]	$\nu_{Q,l}$ [MHz]	δ_l [%]	f_d [%]	$\nu_{Q,d}$ [MHz]	δ_d [%]
RT	66(2)	5.83(6)	17.0(7)	34(1)	9.2(1)	72(3)
350	76(3)	5.94(6)	20.2(6)	24(1)	9.1(1)	46(3)
400	93(7)	6.13(6)	18.4(3)	6.9(5)	8.7(5)	82(7)
500	100	6.86(6)	15.7(2)	0	-	-
600	100	7.27(7)	14.7(2)	0	-	-
700	100	7.52(7)	11.8(2)	0	-	-
800	100	8.11(8)	11.8(3)	0	-	-
900	100	8.46(8)	11.4(2)	0	-	-
RT	66(2)	5.87(6)	15.6(5)	34.5(8)	9.6(1)	73(2)

Tab. A.3: Fit parameters for the undoped sample GN5465 in dependence of the temperature. f_l is the fraction of probes in an undisturbed lattice environment. $\nu_{Q,l}$ and δ_l are the corresponding frequency and damping. f_d is the fraction of probes with a point defect in the nearest neighbourhood with the corresponding frequency $\nu_{Q,d}$ and damping $\delta_{Q,d}$.

Temperature [K]	f_l [%]	$\nu_{Q,l}$ [MHz]	δ_l [%]	f_d [%]	$\nu_{Q,d}$ [MHz]	δ_d [%]
RT	67.2(7)	5.97(6)	15.3(3)	32.7(4)	13.5(1)	86(2)
350	81(2)	6.15(6)	18.8(4)	18.4(4)	13.8(5)	151(9)
400	89(3)	6.09(6)	15.1(4)	11.2(4)	19(2)	234(31)
450	92(3)	6.49(6)	11.8(3)	8.0(3)	24(4)	391(75)
500	92(3)	6.75(6)	10.7(2)	7.9(2)	20(3)	394(53)
700	92(5)	7.50(7)	9.1(3)	7.9(4)	21(3)	188(43)
900	92(5)	8.30(8)	8.4(3)	8.1(4)	24(4)	216(45)
RT	66(1)	5.94(6)	14.3(5)	33.9(6)	13.3(1)	85(3)

Tab. A.4: Fit parameters for the doped sample GN5499 with a concentration of 2×10^{17} atoms/cm^3 in dependence of the temperature. f_l is the fraction of probes in an undisturbed lattice environment. $\nu_{Q,l}$ and δ_l are the corresponding frequency and damping. f_d is the fraction of probes with a point defect in the nearest neighbourhood with the corresponding frequency $\nu_{Q,d}$ and damping $\delta_{Q,d}$.

Temperature [K]	f_l [%]	$\nu_{Q,l}$ [MHz]	δ_l [%]	f_d [%]	$\nu_{Q,d}$ [MHz]	δ_d [%]
RT	68(1)	5.95(6)	16.0(2)	32.4(7)	9.1(1)	86(3)
350	76(3)	6.10(6)	19.8(4)	23.9(8)	8.8(2)	70(3)
400	86(6)	6.22(6)	20.5(4)	14.1(9)	8.5(3)	63(6)
600	100	7.20(7)	20.7(4)	-	-	-
800	100	8.03(8)	19.1(4)	-	-	-
RT	70(1)	5.90(6)	16.6(2)	29.7(8)	9.4(2)	80(3)

Tab. A.5: Fit parameters for the doped sample GN4895 with a concentration of 6×10^{17} atoms/cm^3 in dependence of the temperature. f_l is the fraction of probes in an undisturbed lattice environment. $\nu_{Q,l}$ and δ_l are the corresponding frequency and damping. f_d is the fraction of probes with a point defect in the nearest neighbourhood with the corresponding frequency $\nu_{Q,d}$ and damping $\delta_{Q,d}$.

Temperature [K]	f_l [%]	$\nu_{Q,l}$ [MHz]	δ_l [%]	f_d [%]	$\nu_{Q,d}$ [MHz]	δ_d [%]
RT	73(1)	6.05(5)	16.3(5)	27.1(5)	14.8(2)	46(2)
350	83(3)	6.02(6)	20.5(5)	17.0(6)	11.4(3)	49(3)
400	91(2)	6.11(6)	14.5(4)	9.3(4)	8.2(2)	70(4)
500	100	6.82(6)	11.1(3)	-	-	-
600	100	7.25(7)	9.9(3)	-	-	-
700	100	7.62(7)	9.0(2)	-	-	-
800	100	8.09(8)	7.9(2)	-	-	-
900	100	8.47(8)	7.8(2)	-	-	-
RT	67(1)	6.04(5)	13.1(4)	33.1(5)	14.1(2)	55(2)

Tab. A.6: Fit parameters for the doped sample GN4877 with a concentration of 1.1×10^{18} atoms/cm^3 in dependence of the temperature. f_l is the fraction of probes in an undisturbed lattice environment. $\nu_{Q,l}$ and δ_l are the corresponding frequency and damping. f_d is the fraction of probes with a point defect in the nearest neighbourhood with the corresponding frequency $\nu_{Q,d}$ and damping $\delta_{Q,d}$.

Temperature [K]	f_l [%]	$\nu_{Q,l}$ [MHz]	δ_l [%]	f_d [%]	$\nu_{Q,d}$ [MHz]	δ_d [%]
RT	79(1)	6.89(6)	19.7(3)	21.5(3)	22(1)	276(15)
350	82(2)	6.84(6)	18.4(4)	18.1(4)	48(4)	187(13)
400	84(1)	7.03(7)	15.7(3)	16.1(3)	71(6)	166(20)
450	85(2)	7.18(7)	13.8(3)	15.0(3)	77(7)	136(19)
500	86(2)	7.37(7)	13.3(3)	14.5(3)	68(7)	163(22)
600	86(2)	7.70(7)	13.3(3)	14.4(3)	73(6)	146(19)
800	86(2)	8.4(8)	11.5(2)	14.0(3)	47(4)	173(19)
900	85(2)	8.82(8)	10.4(2)	14.6(3)	43(4)	183(16)
RT	81(2)	6.76(6)	20.8(4)	18.5(2)	28(1)	224(21)

Tab. A.7: Fit parameters for the doped sample GN4876 with a concentration of 3.7×10^{18} atoms/cm^3 in dependence of the temperature. f_l is the fraction of probes in an undisturbed lattice environment. $\nu_{Q,l}$ and δ_l are the corresponding frequency and damping. f_d is the fraction of probes with a point defect in the nearest neighbourhood with the corresponding frequency $\nu_{Q,d}$ and damping $\delta_{Q,d}$.

Temperature [K]	f_l [%]	$\nu_{Q,l}$ [MHz]	δ_l [%]	f_d [%]	$\nu_{Q,d}$ [MHz]	δ_d [%]
RT	83(1)	7.31(7)	23.9(3)	16.1(3)	26(1)	240(16)
350	85(2)	7.52(7)	23.9(4)	15.1(4)	24(2)	291(30)
400	85(2)	7.60(7)	19.(4)	14.5(4)	24(3)	449(55)
450	87(2)	7.70(7)	18.5(3)	12.5(3)	27(3)	517(70)
500	90(3)	7.77(7)	20.1(4)	10.3(4)	28(3)	574(106)
700	89(3)	8.41(8)	18.0(3)	10.9(4)	28(3)	407(62)
900	88(2)	9.2(1)	15.4(3)	11.9(3)	26(3)	327(37)

Tab. A.8: Fit parameters for the doped sample GN4885 with a concentration of 9.2×10^{18} atoms/cm^3 in dependence of the temperature. f_l is the fraction of probes in an undisturbed lattice environment. $\nu_{Q,l}$ and δ_l are the corresponding frequency and damping. f_d is the fraction of probes with a point defect in the nearest neighbourhood with the corresponding frequency $\nu_{Q,d}$ and damping $\delta_{Q,d}$.

B. Spectra

B.1 Annealing behaviour

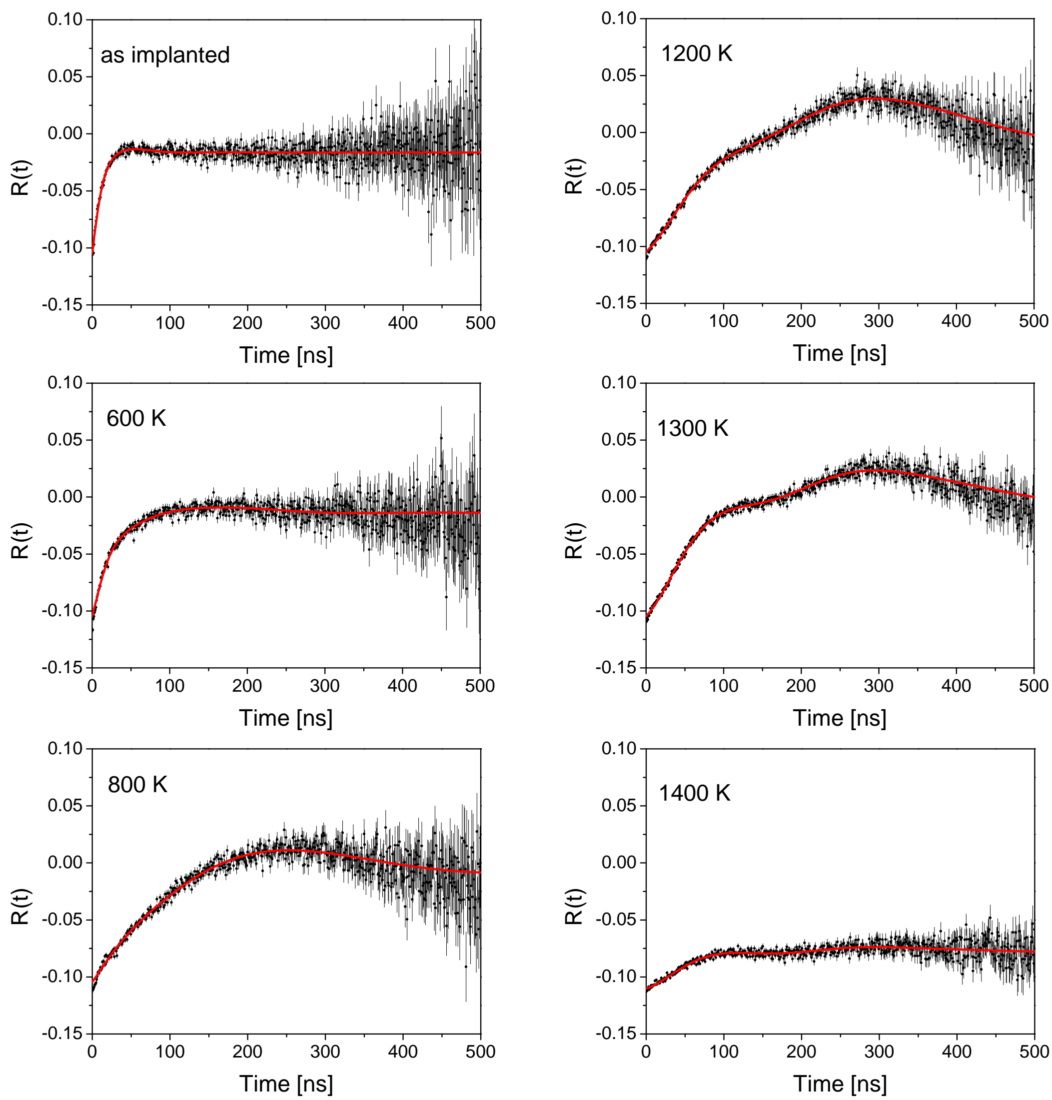

Fig. B.1: The $R(t)$ spectra measured at room temperature after annealing at varying temperature for the undoped GaN sample GN5465.

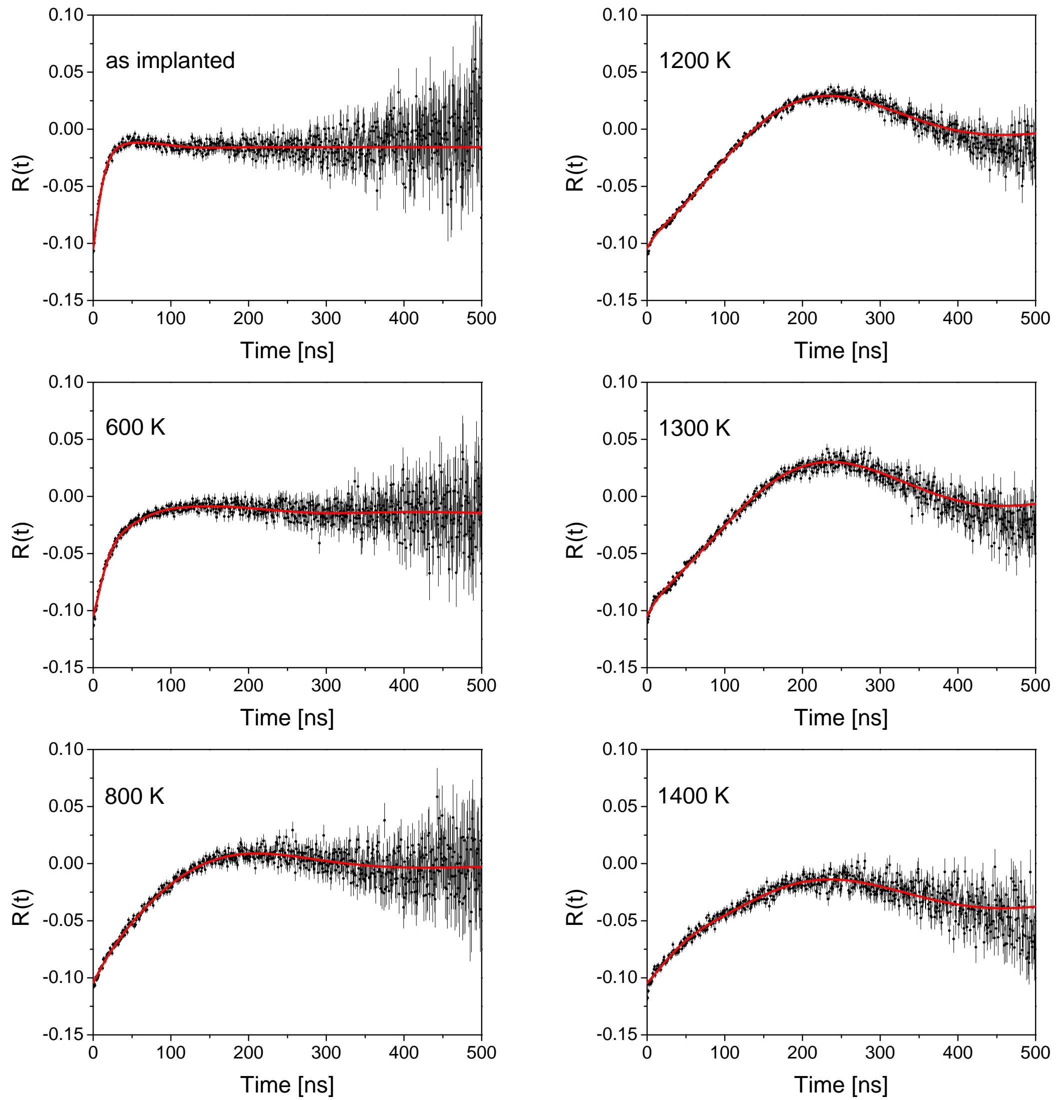

Fig. B.2: The $R(t)$ spectra measured at room temperature after annealing at varying temperature for the doped GaN sample GN4885 with a silicon concentration of 9.2×10^{18} atoms/(cm^3.

B.2 Temperature dependent measurments

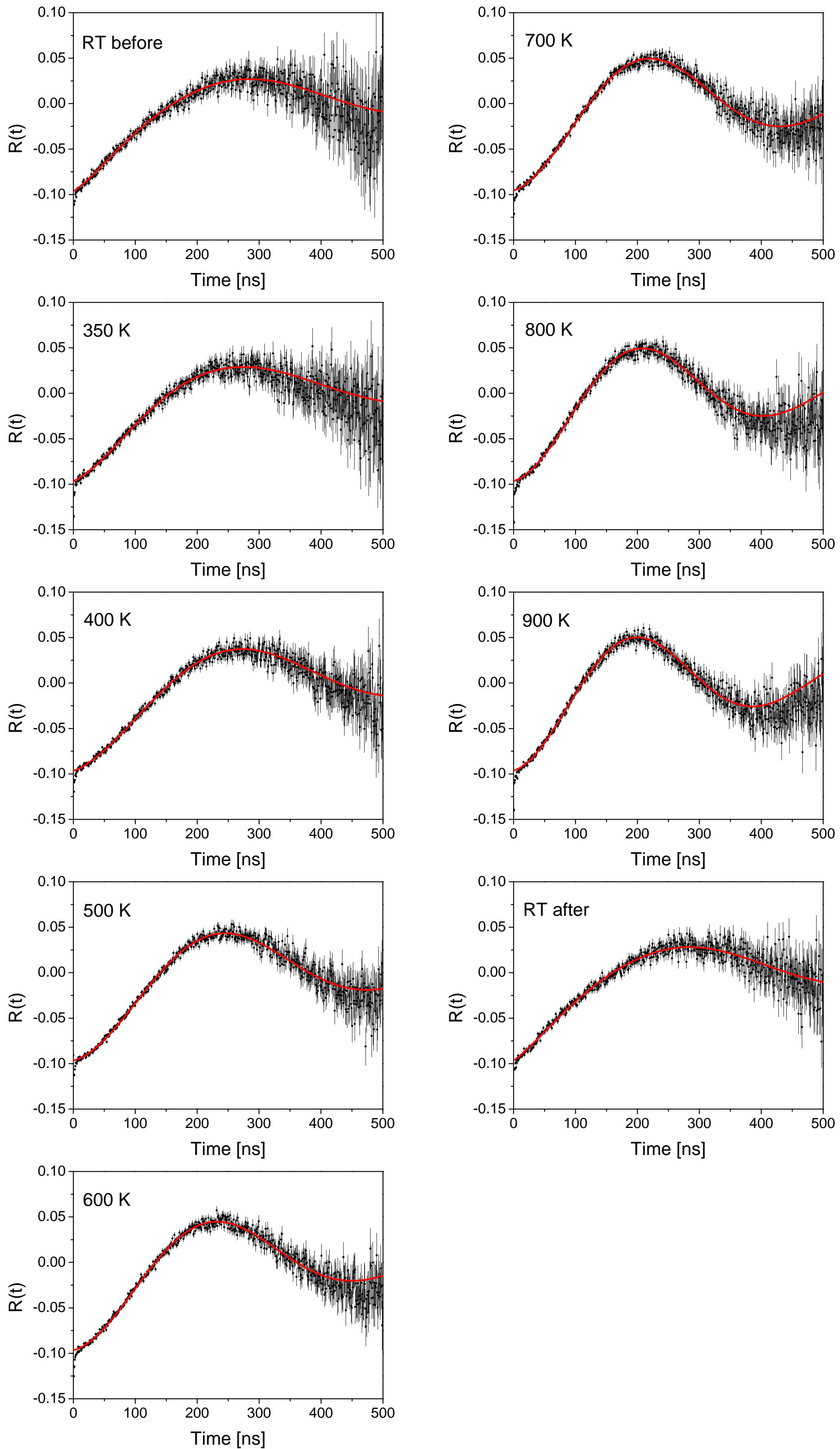

Fig. B.3: The $R(t)$ spectra for the temperature dependent measurements of the pure GaN sample GN5465.

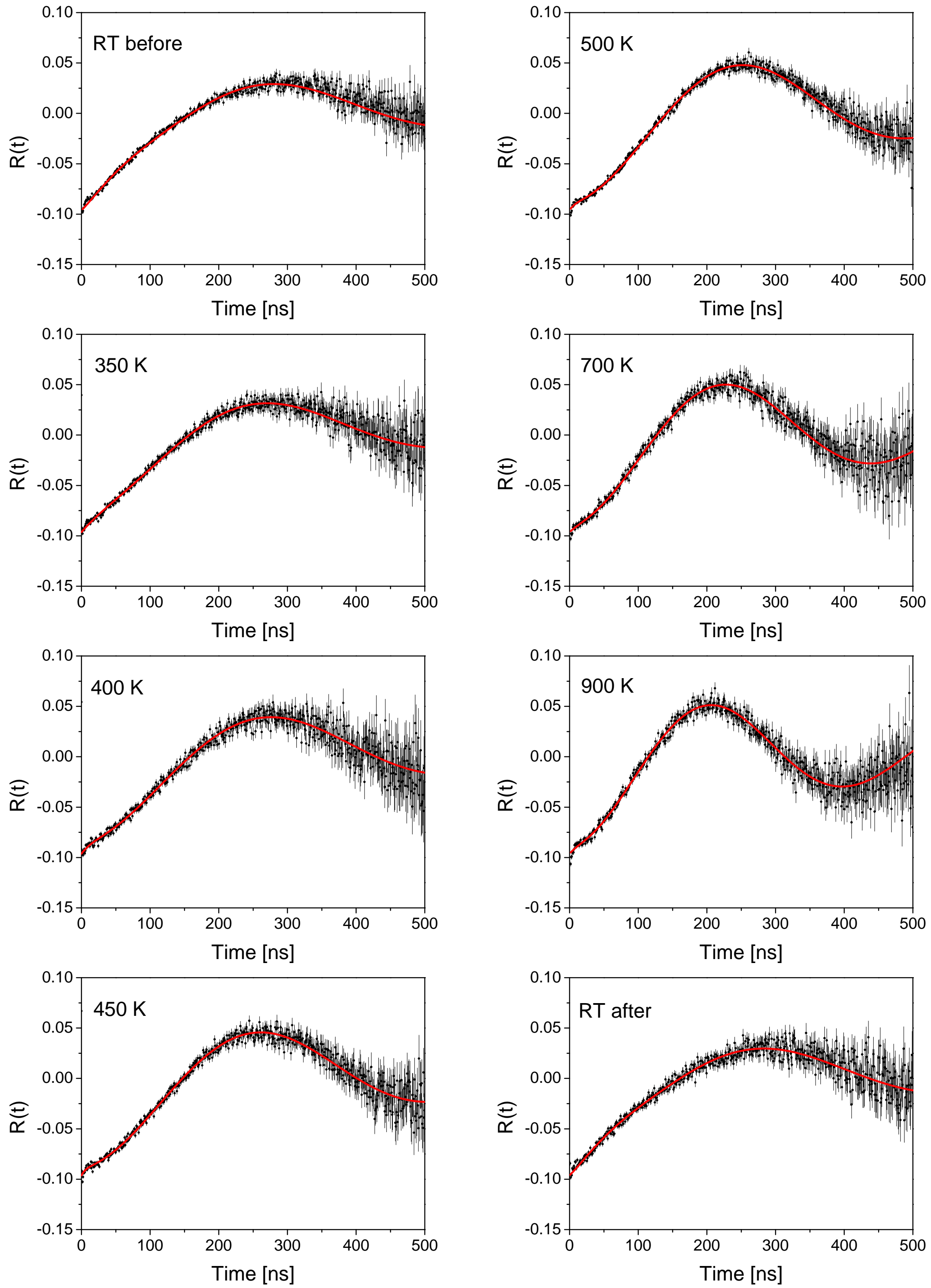

Fig. B.4: The $R(t)$ spectra for the temperature dependent measurements of the GaN-Si sample GN5499 with a silicon concentration of 2×10^{17} atoms/cm^3.

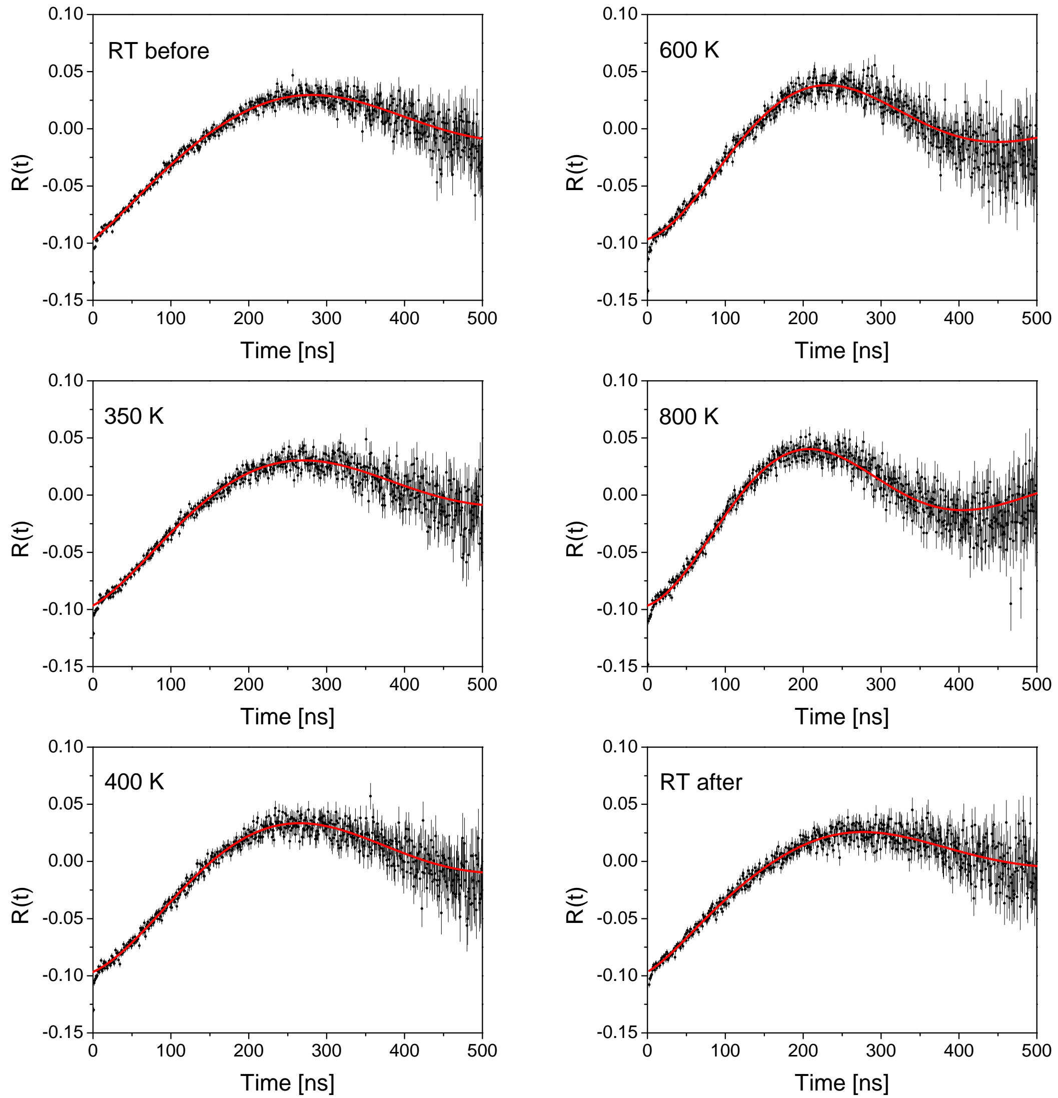

Fig. B.5: The $R(t)$ spectra for the temperature dependent measurements of the GaN-Si sample GN4895 with a silicon concentration of 6×10^{17} atoms/cm^3.

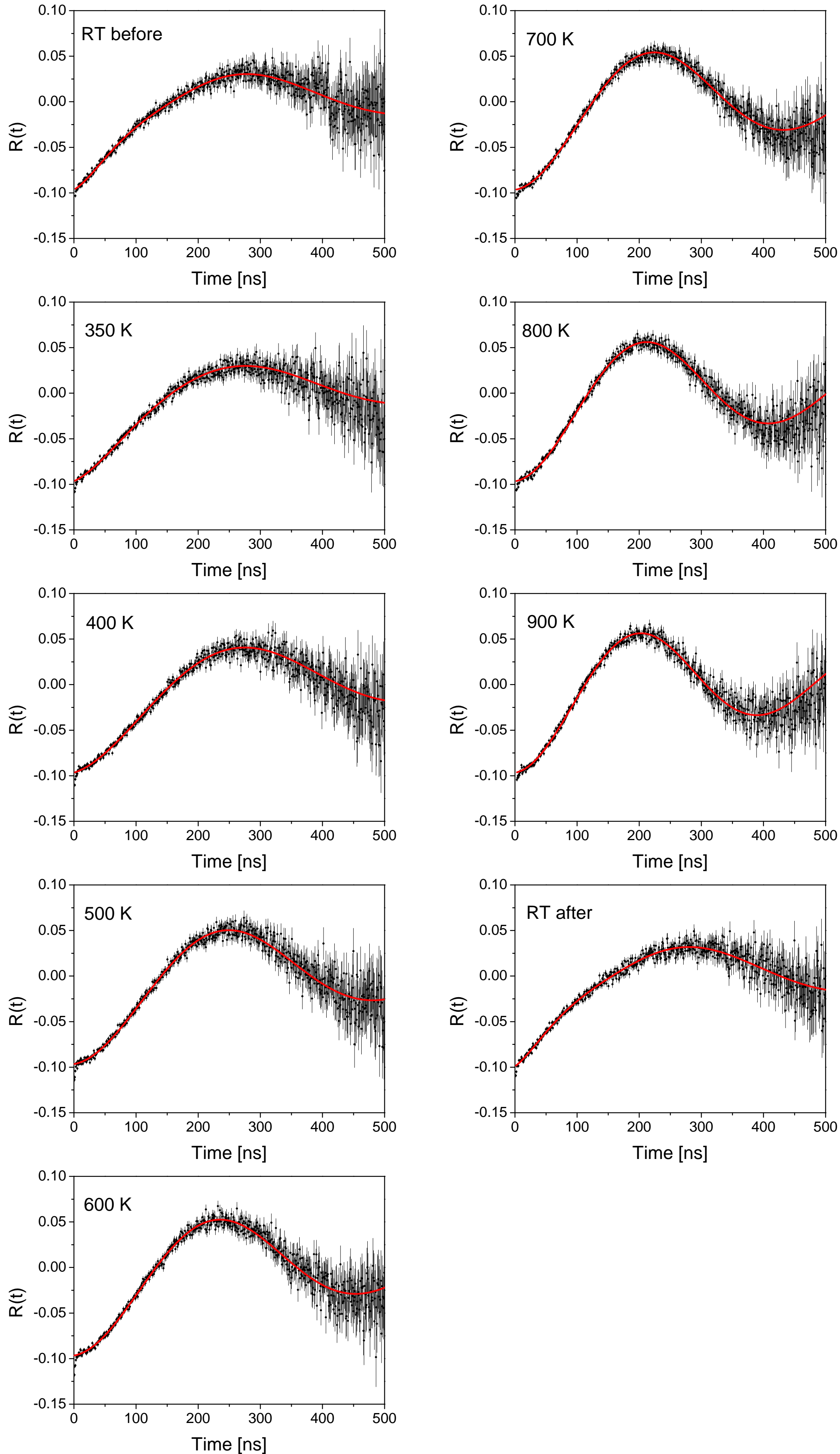

Fig. B.6: The $R(t)$ spectra for the temperature dependent measurements of the GaN-Si sample GN4877 with a silicon concentration of 1.1×10^{18} atoms/cm^3.

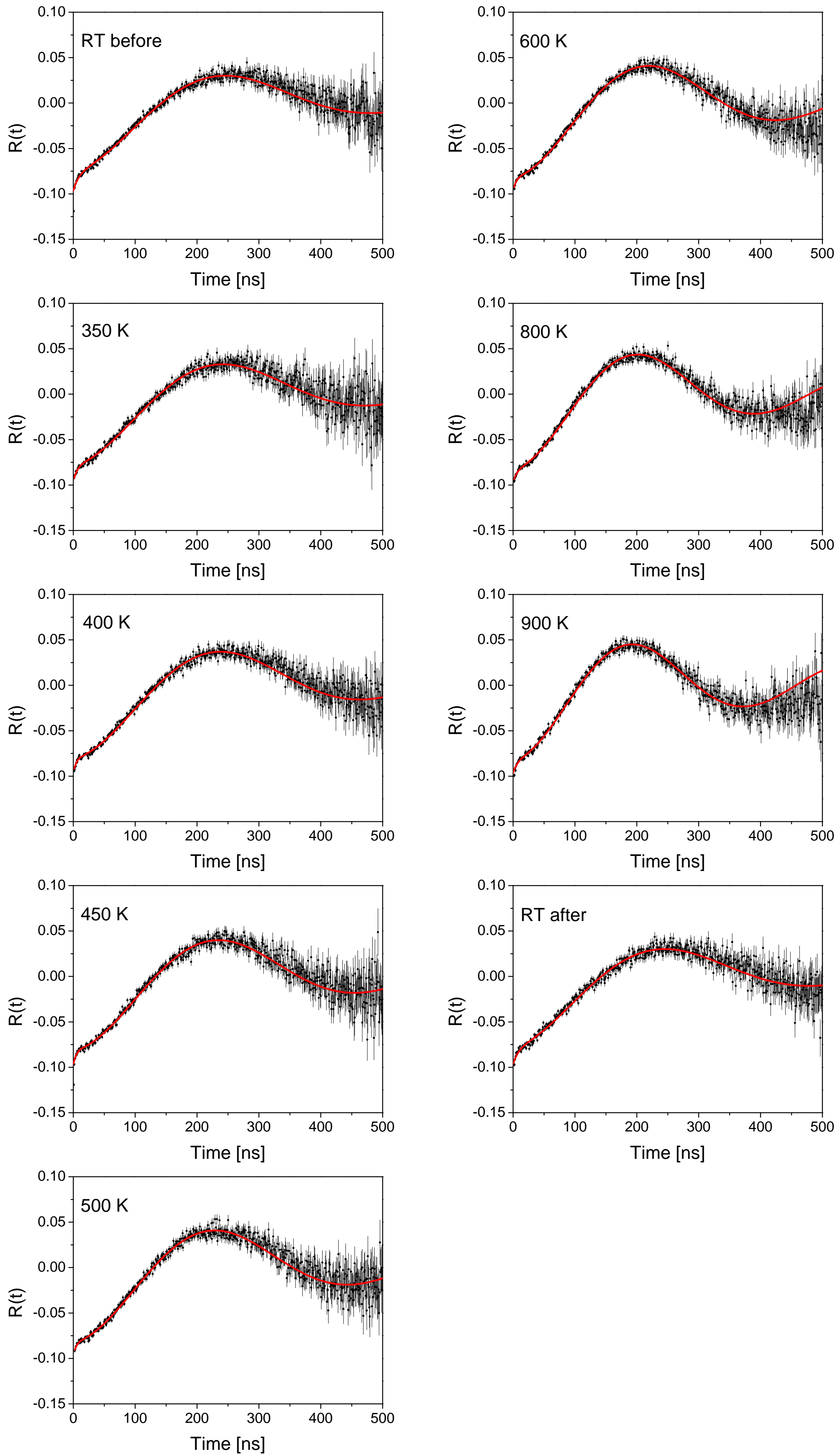

Fig. B.7: The $R(t)$ spectra for the temperature dependent measurements of the GaN-Si sample GN4876 with a silicon concentration of 3.7×10^{18} atoms/cm^3.

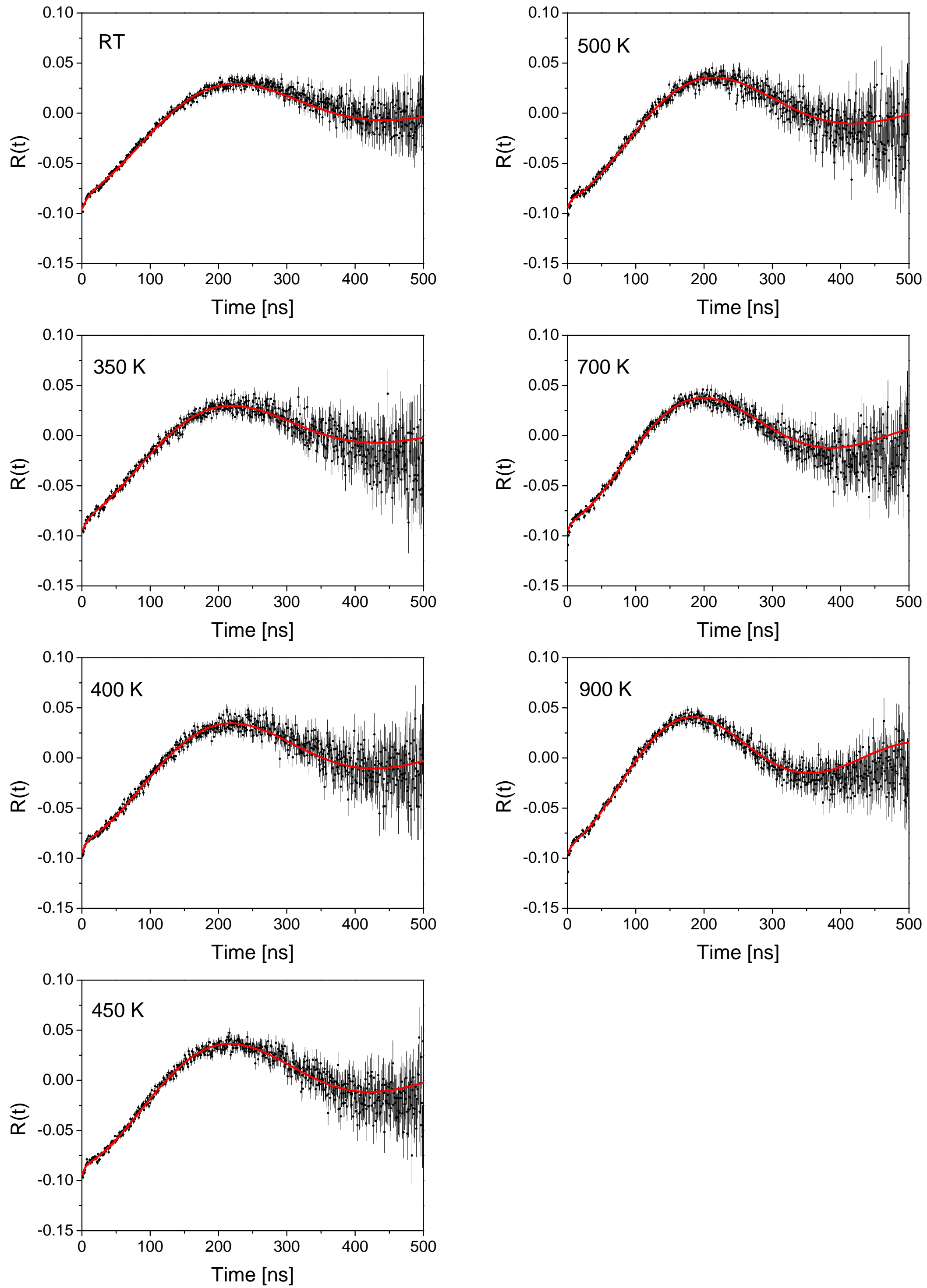

Fig. B.8: The $R(t)$ spectra for the temperature dependent measurements of the GaN-Si sample GN4885 with a silicon concentration of 9.2×10^{18} atoms/cm^3.

Bibliography

[1] H. Morkoç, *Handbook of Nitride Semiconductors and Devices: GaN-based Optical and Electronic Devices*, volume 3, Wiley-VCH, 2008.

[2] S. Chichibu, T. Azuhata, T. Sota, and S. Nakamura, *Journal of Applied Physics* **70**, 2822 (1997).

[3] P. Kessler, K. Lorenz, and R. Vianden, *Defect and Diffusion Forum* **311**, 167 (2011).

[4] M. A. Reshchikov and H. Morkoç, *Journal of Applied Physics* **97** (2005).

[5] W. Götz and N. Johnson, *Applied Physics Letters* **68** (1996).

[6] F. Bechstedt, B. Meyer, and M. Stutzmann, *Group III-Nitrides and Their Heterostructures: Growth, Characterization and Applications*, Wiley-VCH, 2003.

[7] J. C. Nipko, C.-K. Loong, C. M. Balkas, and R. F. Davis, *Journal of Applied Physics* **73**, 34 (1998).

[8] C. Liu, A. Wenzel, B. Rauschenbach, E. Alves, A. Sequeira, N. Franco, M. da Silva, J. Soares, and X. Fan, *Nuclear Instruments and Methods in Physics Research Section B: Beam Interactions with Materials and Atoms* **178**, 200 (2001).

[9] O. Ambacher, *J. Phys. D: Appl. Phys.* **31**, 2653 (1998).

[10] G. Schatz and A. Weidinger, *Nukleare Festkörperphysik*, Teubner, 1997.

[11] K. Siegbahn, *Alpha- beta- and gamma-ray spectroscopy*, volume 2, North-Holland Pub. Co, 1965.

[12] L. C. Biedenharn and M. E. Rose, *Rev. Mod. Phys.* **25**, 729 (1953).

[13] E. Gerdau, J. Wolf, H. Winkler, and J. Braunsfurth, *Proceedings of the Royal Society of London. Series A, Mathematical and Physical Sciences* **311**, 197 (1969).

[14] H. Koch, *Defekt-Fremdatom Wechselwirkung in den hexagonalen Metallen Rhenium und Lutetium*, PhD thesis, Universität Bonn, 1992.

[15] R. Valentini, *Winkelkorrelationsuntersuchungen an Seltenen Erden in Halbleiter mit großer Bandlücke*, PhD thesis, Universität Bonn, 2011.

[16] R. Nédélec, *Seltene Erden in GaN und ZnO untersucht mit der PAC-Methode*, PhD thesis, Universität Bonn, 2007.

[17] F. Ruske, *Indiumimplantation in Galliumnitrid untersucht mit der Gamma-Gamma-Winkelkorrelationsmethode*, Diploma thesis, Universität Bonn, 2001.

[18] A. R. Arends, C. Hohenemser, F. Pleiter, H. de Waard, L. Chow, and R. M. Suter, *Hyperfine Interactions* **8**, 191 (1980).

[19] J. Biersack and L. Haggmark, *Nuclear Instruments and Methods* **174**, 257 (1980).

[20] G. Marx, *Aufbau und Test einer RTA - Kurzzeit-Temper-Anlage*, Diploma thesis, Universität Bonn, 1990.

[21] J. Penner, *Lokale Gitterumgebung von Indium in GaN, AlN und InN*, PhD thesis, Universität Bonn, 2007.

[22] M. Arenz, *Aufbau und Test eines Hochtemperaturmessofens für γ-γ-Winkelkorrelationsmessungen*, Diploma thesis, Universität Bonn, 2010.

[23] M. Steffens, *Hyperfeinwechselwirkung in dünnen Schichten des Gate-Dielektrikums HfO_2*, Diploma thesis, Universität Bonn, 2007.

[24] P. Cojocaru, *Aufbau und Test einer Regelung des Hochtemperaturmessofens für γ-γ-Winkelkorrelationsmessungen*, Diploma thesis, Universität Bonn, 2010.

[25] K. Lorenz, *Implantationsstudien an Gruppe-III-Nitriden*, PhD thesis, Universität Bonn, 2002.

[26] K. Laaksonen, M. G. Ganchenkova, and R. Nieminen, *J. Phys.: Condes. Matter* **21** (2009).

[27] S. Nakamura, M. Senoh, N. Iwasa, and S. Nagayama, *Jpn. J. Appl. Phys.* **31**, 195 (1992).

[28] M. Katsikini, F. Pinakidou, E. C. Paloura, and F. Boscherini, *Journal of Applied Physics* **101**, 083510 (2007).

[29] L. T. Romano, C. Van de Walle, J. W. Ager III, W. Götz, and R. Kern, *Journal of Applied Physics* **87** (2000).

[30] S. Ruvimov, Z. Liliental-Weber, T. Suski, J. W. Ager, J. Washburn, J. Krueger, C. Kisielowski, E. R. Weber, H. Amano, and I. Akasaki, *Applied Physics Letters* **69** (1996).

[31] A. Cremades, L. Görgens, O. Ambacher, M. Stutzmann, and F. Scholz, *Phys. Rev. B* **61**, 2812 (2000).

[32] M. Corti, A. Gabetta, M. Fanciulli, A. Svane, and N. E. Christensen, *Phys. Rev. B* **67**, 064416 (2003).

[33] H. Barfuss, G. Böhnlein, H. Hohenstein, W. Kreische, H. Niedrig, and A. Reimer, *Z. Phys. B - Condensed Matter* **45**, 193 (1982).

[34] K. Köhler, J. Wiegert, H. P. Menner, M. Maier, and L. Kirste, *Journal of Applied Physics* **103** (2008).

[35] M. Leszczynski, T. Suski, H. Teisseyre, P. Perlin, I. Grzegory, J. Jun, S. Porowski, and T. D. Moustakas, *Journal of Applied Physics* **76**, 4909 (1994).

[36] J. Christiansen, P. Heubes, R. Keitel, W. Klinger, W. Loeffler, W. Sandner, and W. Witthuhn, *Z. Phys. B - Condensed Matter* **24**, 177 (1976).

[37] P. Kessler, K. Lorenz, S. Miranda, J. Correia, K. Johnston, and R. Vianden, *Hyperfine Interactions* **197**, 187 (2010).

[38] J. Xie, S. Mita, A. Rice, J. Tweedie, L. Hussey, R. Collazo, and Z. Sitar, *Applied Physics Letters* **98**, 202101 (2011).

Acknowledgement

I would like to take the opportunity to thank those people who spent their time and shared their knowledge for helping me to complete my thesis with the best possible result.

First of all, I would like to thank Priv.-Doz. Dr. Vianden for giving me the opportunity of writing my thesis in his research group. His supervision was excellent and he was always present to answer my questions and to help me in the laboratory. It is due to him that I learned so much during this year. Furthermore, I owe him the research trips to CERN which were a great experience.

I would like thank Prof. Dr. Kai-Thomas Brinkmann who agreed to be the second examiner.

Further I would like to extend my thank to Oliver Ambacher and Klaus Köhler for fabricating the samples.

I would also like to acknowlegde the staff of the isotope seperator. Without them all my measurements would not have been possible.

Special thanks go to all members of our research group. They made this year a great experience. Only due to their help and support I was able to complete this thesis. In particular, I would like to thank Patrick Keßler and Michael Steffens for proofreading my thesis and Marius Arenz for helping me with all software related problems and editing plots. A big thank you also goes to Christian Karrasch who was not only a funny room mate in Dresden and Leuven but has become a close friend.

I would like to thank the research group of Prof. Dr. Karl Maier for the coffees and barbecues we shared.

Many thanks go to all fellow students who I got to know during my studies. It is due to them that this time is worth remembering.

Finally, I would like to thank my parents for their unlimited support. Without their help my study at a university would not have been possible. I cannot forget to express appreciation to my sweetheart Jessica who is always able to cheer me up with her cuteness.

Declaration

I hereby certify that the work presented here was accomplished by myself and without the use of illegitimate means or support, and that no sources and tools were used other than those cited.

Bonn, ... Signature: ....